Establishing Microstructure - Electron Work Function - Property Relationships towards a New Design Methodology for Structural Materials

by

Yuzhuo Luo

A thesis submitted in partial fulfillment of the requirements for the degree of

Master of Science

in

Materials Engineering

Department of Chemical and Materials Engineering
University of Alberta

Abstract

Conventional metallurgy has been widely used in material design for centuries, which however does not always effectively guide material design and modification. A large number of trial-and-error tests are often needed in material development. Material developers have been making considerable efforts in developing complementary or alternative approaches to guide material design. Attributed to the intrinsic correlation between electron work function (EWF) and the atomic bond strength and stability, which govern mechanical and electrochemical properties of materials, EWF has been demonstrated to be a promising guiding parameter for material analysis and design. Many intrinsic properties of metals such as Young's modulus, thermal expansion coefficient, and electrochemical activity, etc., can be well correlated with EWF theoretically, confirmed by experimental studies. For pure metals and single-phase solid solutions, the higher the EWF of a material, the higher atomic bond strength with higher mechanical stability. However, engineering materials are generally multi-phase materials. It is unclear whether or not the overall EWF of multiphase materials with specific microstructure features can still reflect the material properties. In this study, two-phase high-Cr cast irons were used to investigate microstructure-EWF-property relationships. A charge-compensation model was established to elucidate the mechanism responsible for such relationships. It turned out that fine and densely distributed second phase, i.e. the carbide in the ferrous matrix, contributed to higher interfacial/volume ratio, leading to charge redistribution at interface. Such charge redistribution at interface results in increased overall EWF, corresponding to elevated Young's modulus. For further information and verification, low carbon steels with two-

level microstructural complexity were used to verify the microstructure-EWF-property relationships and the charge-compensation model. Various experimental tools, including Scanning Kelvin Probe, Atomic Force Microscope, Scanning Electron Microscope, Transmission Electron Microscope and acoustic instrument etc., were used to investigate the effect of microstructure on overall EWF and corresponding properties of the steels. It was demonstrated that the properties of steel samples, including Young's modulus, hardness and corrosion resistance, can be well reflected by their overall EWFs and explained based on the charge-compensation model. The calculated theoretical EWF was in consistent with experimental results. This study is of significance to the extension of utilizing EWF in structural materials design from single-phase materials to multi-phase ones.

Preface

This thesis is an original work carried out by Yuzhuo Luo, supervised by Dr. Dongyang Li. Results of first-principles calculation in Chapter 3.2.5 are provided by Dr. Yunqing Tang, Department of Chemical and Materials Engineering, University of Alberta. Atomic force mapping in Chapter 3.2.3 was assisted by Dr. Liqiu Guo, Department of Chemical and Materials Engineering, University of Alberta. Optical, SEM and TEM images of low carbon steel in Chapter 4.2.1 was assisted by Tsai-Fu Chung and Jer-ren Yang, Department of materials Science & Engineering, National Taiwan University.

Acknowledgement

I am very grateful to Dr. Dongyang Li for his meticulous help in my graduate academic journey. He guides the experimental direction with patience, provides suggestions on critical issues and helps to modify all the materials, making me have a deeper understanding in the field of metallic material.

Also, I want to thank all the lab mates in Dr. Dongyang Li's group, for the guidance and support on daily life. I would like to thank Dr. Liqiu Guo for teaching atomic force mapping technology, Dr. Yunqing Tang for conducting first-principle calculations, Dr. Mingyu Wu for helping electrochemical experiments, Mr. Runfang Hou and Ms. Jiaqi Li for machine instruction and daily help.

I appreciate all the faculty staff of Chemical and Materials Engineering in University of Alberta, and cherish the opportunity to work with such excellent fellows. I also thank committee members who make suggestions on my research.

Finally, I want to thank my family and all the friends I met in Edmonton. We encouraged each other and shared happiness. May everyone have a bright future.

Table of Contents

List of Tables

List of Figures

List of Symbols

Symbols are arranged in the order of appearing in the thesis.

φ	Electron work function
V_c	Contact potential
V_b	Reverse potential
E_k	Kinetic energy
E_f	Fermi level
n	Electron density
ε_0	Vacuum permittivity
e	Elementary charge
$\hbar$	Planck's constant
m	Mass of electron
E	Young's modulus
ε_b	Bond energy
α	Madelung constant
a	Lattice constant
G	Shear modulus

υ	Poisson's ratio
B	Burgers vector
ξ	Width of dislocation
r_s	Wigner-Seitz radius
γ_i	Surface energy
K_W	Wear coefficient
F	Load
H	Hardness
ρ_e	Electron density
σ	Interfacial charge density
S	Interfacial area
V_m	Volume of matrix
$\Delta\rho_{e-}$	Change in the free electron density of matrix
x	Half the width of the dipole layer
E_{corr}	Corrosion potential
j_{corr}	Corrosion current density
I_{corr}	Corrosion current

List of Abbreviations

AFM	Atomic Force Microscope
ASTM	American Society for Testing and Materials
CPD	Contact Potential Difference
CR	Corrosion Rate
DFT	Density Functional Theory
ELF	Electron Localization Function
EW	Equivalent Weight
EWF	Electron Work Function
GGA	Generalized Gradient Approximation
HCCI	High-Cr Cast Irons
KPFM	Kelvin Probe Force Microscopy
LCA	Low Carbon Steel with Annealing
LCN	Low Carbon Steel with Normalizing
OCP	Open Circuit Potential
PBE	Perdew-Burke-Ernzerhof
SCE	Saturated Calomel Electrode

SEM	Scanning Electron Microscope
SKP	Scanning Kelvin Probe
TEM	Transmission Electron Microscope
UPS	Ultraviolet Photoelectron Spectroscopy
VASP	Vienna Ab-initio Simulation Package
XRD	X-ray Diffraction

Chapter 1 Introduction

With the rapid technological development, the demand for high performance metallic materials is increasing. Materials can be improved through microstructural engineering. Traditional metallurgy has been widely applied to guide modification of metallic materials for optimized properties. However, the conventional metallurgy is not always effective, an immense amount of trial - and - error tests are often required to collect essential data, which is time-consuming and costly. It is desired to explore complementary or alternative, and fundamental approaches for material design and modification. It is known that the intrinsic mechanical properties of materials are largely dependent on the electron state and atomic bond strength (*1*). The electron density and energy state could be useful in material analysis, but it is complicated and not convenient for engineers to use them in material design. It is thus highly wished to have fundamental and feasible parameters, which can reflect electron behavior and bond strength, for guiding material development.

Electron work function (EWF) is such a parameter which represents the minimum energy needed to extract electron from inside a metal at the fermi level to its surface (*2, 3*). Although EWF is dependent on surface condition, intrinsically it reflects interaction strength between nucleus and electrons, which is related to bulk properties (*4*). As a fundamental electronic parameter, EWF has already been correlated with atomic properties (electronegativity and ionization energy etc.) (*2, 5, 6*), which lays a theoretical foundation for application of EWF in material design. EWF has been shown to be correlated with many mechanical properties, such as Young's modulus (*7*), yield strength, hardness (*8*) and

toughness (*9*) etc. Using Young's modulus as an example, EWF and Young's modulus of pure metals have a theoretical six power relationship (*7*). The experimental data on Young's modulus and EWF of pure metals fit well with theoretical model. In addition to the mechanical properties, EWF also reflects physical parameters of materials, such as surface energy (*10*), adhesion (*11, 12*) and friction (*13*), which play crucial roles in tribology and wearing process. With in-depth researches on EWF, properties of multi-elements solid solutions can be modified due to the dependence of their properties on EWF (*14*). Homogeneous Cu-Ni alloy has been investigated to determine if the overall EWF reflects properties of the alloy (*15-17*). The relationship between Young's modulus and EWF for the isomorphous alloy shows good fit with the Young's modulus-EWF curve for pure metals (*15*). The overall EWF of Cu-Ni alloy increases by adding Ni which has a higher EWF, leading to a stronger average atomic bond in the system, and a higher barrier to any change in the current mechanical state. With a higher EWF, the Cu-Ni alloy shows correspondingly increased wear resistance and hardness (*16*). The corrosion resistance of the Cu-Ni alloy also increases due to elevated electrochemical stability with a more stable electron state (*17*).

Up to date, most studies are focused on pure metals and isomorphous solid solutions without microstructural complexity. Whether multiphase metallic materials have similar EWF - property relationship and how microstructure of multiphases synergistically affect overall EWF are unknown. This is the main barrier for EWF to be used in realistic material design involving microstructural complexity (*18-20*). The microstructural factors mutually interact and the overall material properties are integrated from those of individual phases (*21, 22*). When two phases having different EWFs are in contact, an interphase boundary

is formed between two adjacent phases (*11, 23*). As electrons tend to move from low-potential regions, e.g., the metallic matrix, to high-potential regions such as carbides in a cast iron, equivalently the matrix becomes positively charged, making electrons harder to escape from the matrix. We may hypothesize that the matrix would be in a more stable electronic state, corresponding to a higher EWF. The driving force for charge redistribution at interphase is the potential difference (or the difference in EWF) between phases, and formed depletion layer would balance the potential difference with increasing electron stability. Mosleh-Shirazi has observed increased EWF of Al-SiC nanocomposite (*24*). When nano-sized SiC is added to Al matrix, the corrosion resistance of nanocomposite increases. The first-principles calculation indicates that electrons localized at SiC-Al interfacial region, which hinders electrons to participate in corrosion reactions. Hao Lu et al. also report similar results of a study on carbon steel alloyed with Ni (*25*). All the studies indicate that interphase boundary plays an important role. Thus, how the microstructure influences the overall EWF needs to be investigated.

In this thesis study, the effects of microstructure on EWF and corresponding properties of two-phase alloys are investigated. This thesis consists of the following parts: Chapter 1 & 2 provide background information and relevant studies about EWF and its potential application in material design. An established microstructure - EWF - property theoretical model is described in Chapter 3, in which high-Cr cast irons are used as a simple material to verify this model. Chapter 4 presents studies on low carbon steels, which has two levels of microstructural inhomogeneity achieved by adjusting the cooling rate. Differences in microstructure and property among samples are analyzed and linked to EWF as a bridge, which helps develop the microstructure - EWF - property model for multiphase

material design. Finally, Chapter 5 gives general conclusions of this study and potential follow-up studies.

Chapter 2 Literature review

In this chapter, EWF is introduced and its correlation with mechanical properties of pure metals and homogeneous alloys is illustrated. Some experimental observations related to EWFs of multiphase metallic products and corresponding properties are also presented.

2.1 Introduction to EWF

In the early 20th century, people became interested in the electron behavior and believed that it governed the properties of material. Since then, a large number of fundamental rules about the electron behavior has been established based on the development of quantum mechanics (*26-28*). The quantum mechanics is effective to deal with problems but not feasible to guide material design. Researchers also looked for other parameters that may reflect the electron behavior which were easy to be utilized. EWF is one of such parameters. The concept of EWF was developed in early 20th (*29, 30*) and after that, researchers were trying to figure out how to apply EWF in material analysis, mainly for semiconductors and defects. Recent studies show that EWF is also a promising parameter for material design (*7*).

2.1.1 Definition of EWF

EWF (electron work function) represents the minimum energy required to move electrons from inside a metal at Fermi level to its surface (*2, 31*). Fermi level is considered as a hypothetical energy level, which has a 50% possibility of being occupied at any given time (*32*). The position of fermi level inside metal plays a crucial role in determining

electronic properties under the thermodynamic equilibrium condition. The vacuum level represents the energy of a free stationary electron outside a metal surface, taking as infinite position far away from inside the metal (*33*). As shown in figure 2.1, EWF is represented as potential energy difference between fermi level and vacuum level, which is represented as:

$$\varphi = -\mu + D \tag{2.1}$$

where μ is bulk chemical potential of electrons inside a metal, and D represents the energy needed to penetrate the dipole barrier (*34, 35*). One can well perceive that the value of EWF is largely dependent on surface condition, this lays a theoretical foundation for EWF to be used in corrosion behavior (*17, 24, 36, 37*), and adsorption (*38, 39*) etc. Although EWF is largely dependent on the electron behavior at surface, intrinsically it reflects interaction strength between nucleus and electrons, which is related to bulk properties (*4*). The details about the connection between EWF and bulk properties will be described later.

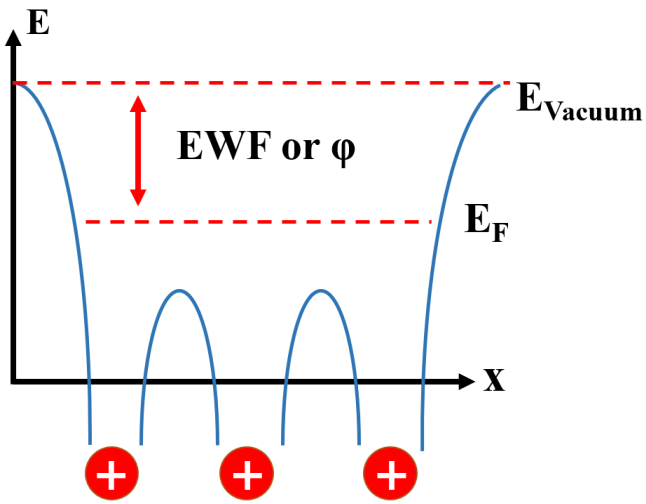

Figure 2.1 Schematic diagram of EWF

2.1.2 Measurement of EWF

Scanning kelvin probe (SKP) and ultraviolet photoelectron spectroscopy (UPS) are commonly used to measure EWF. SKP technology stems from parallel plate capacitor experiments conducted by Lord Kelvin (*40*). As a non-contact, non-destructive technique, SKP is widely used in corrosion and coating analysis. The probe is placed at the top of the sample and a current is applied to form a parallel plate capacitor. A difference in Fermi level is presented in figure 2.2A when two different materials are in contact. When a connection is formed (figure 2.2B), the electron flow moves from material having a higher Fermi energy level region to that having a low Fermi energy level, until their Fermi levels become equal. A potential difference is formed between probe and sample, which is also called contact potential (V_c) (*41*). In order to get the contact potential difference between probe and sample, reverse potential (V_b) is applied to neutralize the charge difference between two parts (figure 2.2C) (*42*). The Fermi level of the sample returns to its original position once local charge changes to zero. Thus, we get:

$$V_b = -V_c \tag{2.2}$$

and this is how SKP technology analyze EWF of samples by comparing the standard EWF of the probe (*43*). It is not hard to see that this technique requires clean surface and oxidation products on surface need be avoided.

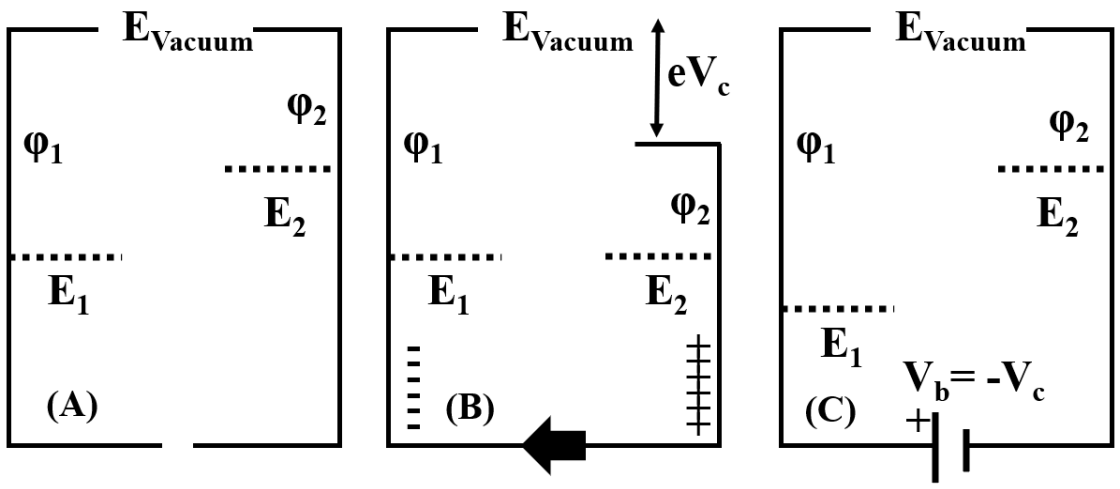

Figure 2.2 (A) Status before the electron flow is connected between sample and probe, (B) Status after the electron flow is connected between sample and probe, (C) Status when reverse potential (V_b) applied to the system

Regarding the UPS method, in short, UPS measures the bonding energy from the highest kinetic energy (from Fermi level) to the lower kinetic energy cutoff as shown in figure 2.3. On the cutoff region of the spectrum, electrons have just enough energy to overcome the potential barrier. EWF can be represented as:

$$\varphi = \mathrm{hv} - E_k \tag{2.3}$$

where E_k represents kinetic energy and hv is input energy of ionizing light. UPS is more like an absolute method of measuring EWF, while SKP is a relative method (*44*).

With the development of atomic force microscope (AFM), kelvin probe force microscopy (KPFM) was added as a function of AFM mapping (*45, 46*). It is also called surface potential microscope with non-contact technology. When sample and tip having different EWFs are in contact, electric flow would form between the two parts and contact

potential difference (CPD) is generated. To calculate EWF, the electrostatic force between sample and tip is analyzed. KPFM is widely used in analyzing local EWF as the *in situ* mapping can be well connected with topography condition (*11, 47*). It is also one of the key methods used in this study and detailed information will be discussed later.

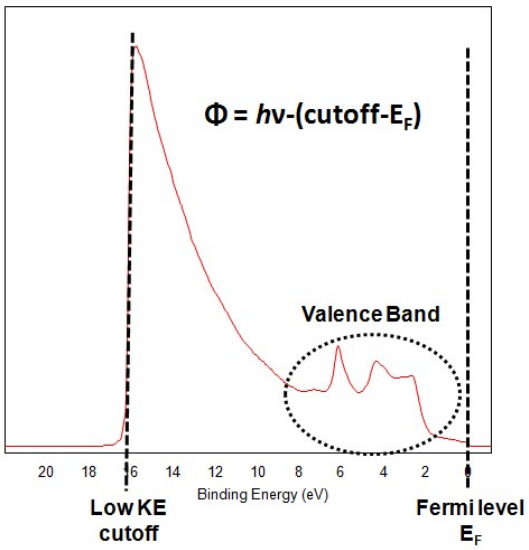

Figure 2.3 UPS spectrum

2.2 Relationship between EWF and intrinsic properties

2.2.1 Image charge model of EWF

The image charge model of EWF has gradually been accepted by the researchers, which assumes the valence electron is located at the center of the arranged structure as shown in figure 2.4A. Based on the definition of EWF in electrostatics, the energy required to prevent moving an electron from surface to infinity under image charge attractive force can be represented as:

$$\varphi = \int_d^{\infty} \frac{e^2}{4\pi\varepsilon_0(2r)^2} dr = \frac{e^2}{16\pi\varepsilon_0 d} \tag{2.4}$$

where d is initial distance as shown in figure 2.4B, r represents the instantaneous distance in the process of moving electron away from surface (*7, 48*). According to the expression of Debye length (D) in plasma physics (*32*):

$$D = \sqrt{\frac{2\varepsilon_0 E_f}{3ne^2}} = \frac{d}{\sqrt{3}} \tag{2.5}$$

So EWF can be expressed with fermi level (E_f) and electron density (n):

$$\varphi = \frac{e^2}{16\pi\varepsilon_0}\sqrt{\frac{ne^2}{2\varepsilon_0 E_f}} \tag{2.6}$$

To simplify this expression, fermi level can also be replaced by electron density as $\hbar$ is Planck's constant and m represents mass of electron:

$$E_f = \frac{\hbar^2(3\pi^2 n)^{2/3}}{2m} \tag{2.7}$$

Thus, we get the expression of EWF related with electron density (*7*):

$$\varphi = \frac{e^3 m^{1/2} n^{1/6}}{16^3\sqrt{3}\pi^{5/3}\hbar\varepsilon_0^{3/2}} \propto n^{1/6} \tag{2.8}$$

This laid a foundation for the theoretical derivation of relationships between EWF and a series of parameters.

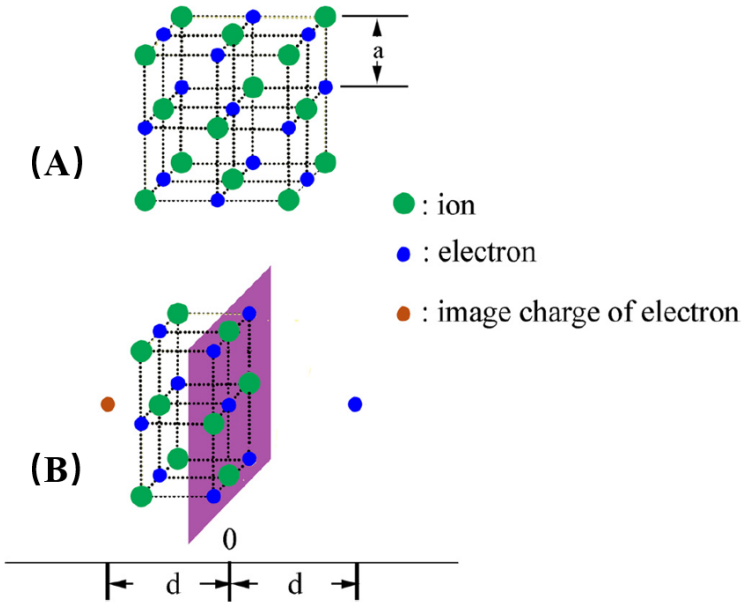

Figure 2.4 (A) Electrons and irons alternately arranged with distance of a, (B) Electrons and its image charge located symmetrically in cubic point arrays (7)

2.2.2 Atomic bond strength

From our previous deduction, Young's modulus can be expressed as (*49*):

$$E = \frac{k}{r_e} \propto \frac{\varepsilon_b}{r_e^3} \tag{2.9}$$

where ε_b represents the bond energy, r_e is equilibrium distance between two adjacent atoms. Based on the image charge model, Young's modulus also has a six-power relationship with EWF (*7*):

$$E \propto \varphi^6 \tag{2.10}$$

The following equation correlates relationship between bond energy and EWF:

$$\varphi^6 = \xi \times \frac{\varepsilon_b}{r_e^3} \tag{2.11}$$

where ξ is determined by experimental data from pure metals. As shown in figure 2.5, the EWF has a theoretical six-power relationship with bond energy, the experimental data correlates well with theoretical model (*49*). More researches indicate that atomic size also has a secondary polynomial relationship with EWF, due to an increasing atomic bond strength with smaller spacing between adjacent atoms (*50*).

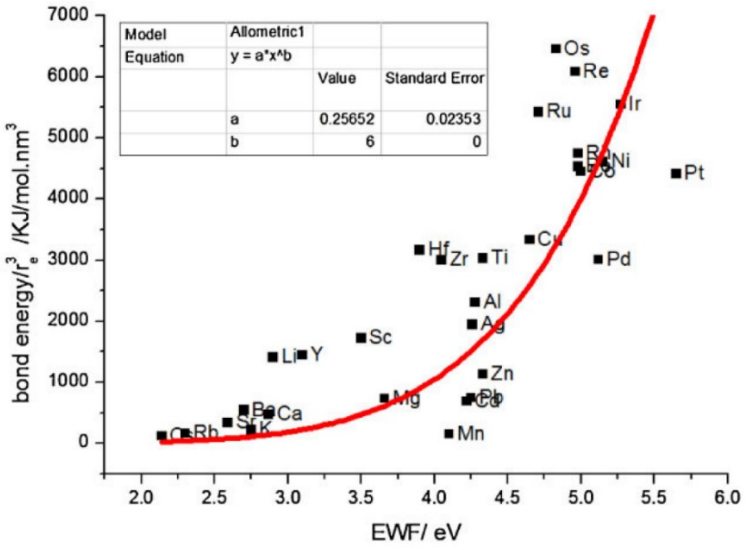

Figure 2.5 Relationship between atomic bond energy and EWF, units are KJ/(mol×nm³) and eV respectively (*49*)

2.2.3 Mechanical parameters

2.2.3.1 Young's modulus

Young's modulus describes the ability of a solid material to resist deformation. To simplify the expression, Madelung energy is formulated as (*7*):

$$U(a) = -\frac{N\alpha z^2 e^2}{a}\left(1 - \frac{\rho}{a}\right) \tag{2.12}$$

where α is Madelung constant, N is number of metal irons, z is number of valence electrons, a is equilibrium distance as shown in figure 2.4. ρ represents the repulsive interaction distance. By neglecting the repulsive interaction when the distance increases, interaction potential is presented as:

$$u = \frac{\alpha z e^2}{a} \tag{2.13}$$

Since Young's modulus is determined by second derivation of interaction potential with regarding to distance (*51*), Young's modulus is expressed with equilibrium distance (a):

$$E = \frac{d^2 u(r)}{dr^2} = \frac{2\alpha z e^2}{a^3} \tag{2.14}$$

Based on previous equation (2.8), when electron density is replaced by lattice distance (*52*),

$$n = \frac{z}{a^3} \tag{2.15}$$

expression of EWF can be rewrite as:

$$\varphi = \frac{e^3 m^{1/2} z^{1/6}}{16^3 \sqrt{3} \pi^{5/3} \hbar \varepsilon_0^{3/2} a^{1/2}} \tag{2.16}$$

Finally, Young's modulus is related with EWF based on a six-power expression (*7*):

$$E = 2\alpha z e^2 \left(\frac{e^3 m^{1/2} z^{1/6}}{16^3 \sqrt{3} \pi^{5/3} \hbar \varepsilon_0^{3/2}}\right)^{-6} \varphi^6 \propto \varphi^6 \tag{2.17}$$

Figure 2.6 shows experimental data on Young's modulus and EWF of pure metals with black dots, which fits well on theoretical model (*53, 54*).

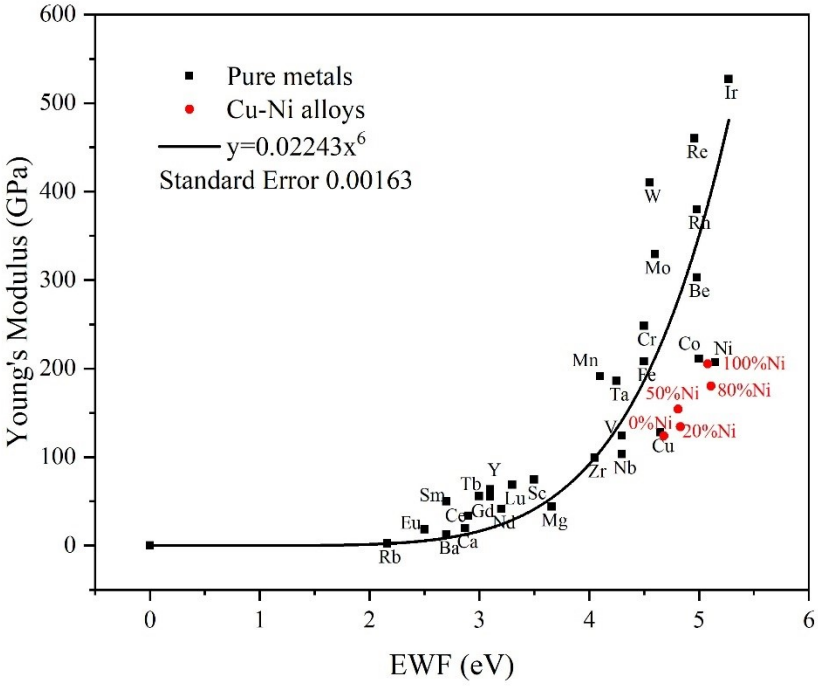

Figure 2.6 Relationship between Young's modulus and EWF on pure metals (black dots) and Cu-Ni alloy (red dots)

2.2.3.2 Yield strength

Yield strength is defined as the yield limit of metallic materials when dislocation occurs, which represents the critical stress that resists a small amount of plastic deformation. In the viewpoint of atomic bond strength, yield strength can be expressed as (*8, 55*):

$$\sigma_y = \frac{2G}{(1-\upsilon)\cos\theta\cos\varphi}\exp\left(-\frac{4\pi\xi}{B}\right) \tag{2.18}$$

where G is shear modulus, υ is Poisson's ratio, θ and φ represents angles of slip direction and slip plane normal respectively. B is Burgers vector. ξ represents width of a dislocation and relates with lattice constant a:

$$\xi = \frac{a}{2(1-\upsilon)} \tag{2.19}$$

In addition, shear modulus can be well related with Young's modulus:

$$G = \frac{E}{2(1+\upsilon)} \tag{2.20}$$

We get the expression of yield strength:

$$\sigma_y = \frac{E}{(1-\upsilon^2)\cos\theta\cos\varphi}\exp\left(-\frac{4\pi\xi}{B}\right) \tag{2.21}$$

Based on previous relationship between Young's modulus and EWF in Chapter 2.2.3.1, yield strength has a six-power relationship with EWF as well (*8*):

$$\sigma_y \propto \frac{1}{(1-\upsilon^2)\cos\theta\cos\varphi}\exp\left(-\frac{4\pi\xi}{B}\right)\varphi^6 \tag{2.22}$$

Figure 2.7 gives experimental data on yield strength of pure metals, which fits well with theoretical model.

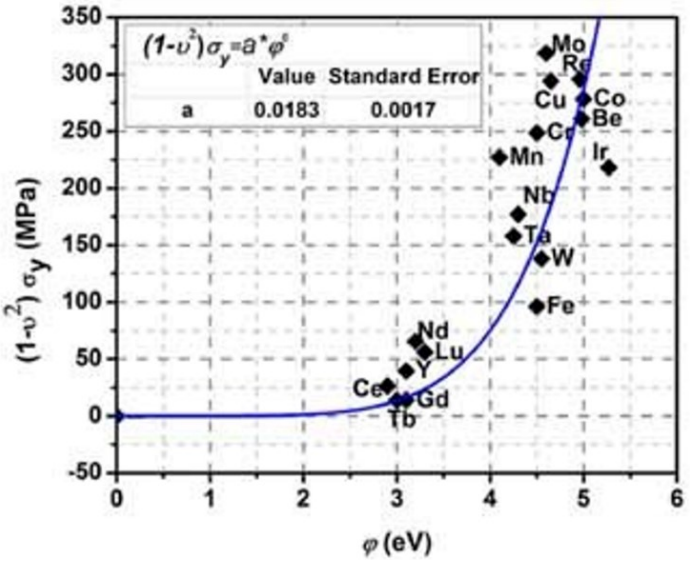

Figure 2.7 Relationship between yield strength and EWF on pure metals (*8*)

2.2.3.3 Hardness

The resistance to localized plastic deformation induced by mechanical indentation or abrasion is called hardness, which is one of the most fundamental mechanical parameters in engineering design. In general, hardness can be proportional related with yield strength (*56*). Based on results from Chapter 2.2.3.2, hardness can be related with EWF through yield strength:

$$H \propto c\frac{1}{(1-\upsilon^2)\cos\theta\cos\varphi}\exp\left(-\frac{4\pi\xi}{b}\right)\varphi^6 \qquad (2.23)$$

where c is determined by structure of indenter geometry. Figure 2.8 shows relationship between intrinsic hardness (material in annealed state) and EWF of transition metals, the experimental data correlates well with theoretical trend (*8*). Although hardness is influenced by many factors such as methods of heat treatment and cold working at surface,

dislocation density still plays a main role on hardness. Stronger atomic bond strength is established based on higher EWF, which can increase the resistance of dislocation movement and electron rearrangement. This makes EWF a potential parameter on guiding hardness of material.

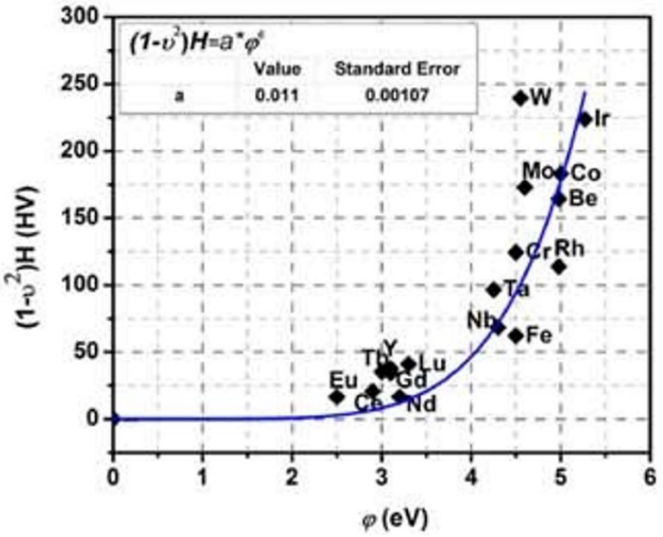

Figure 2.8 Relationship between hardness and EWF (*8*)

2.2.4 Other physical and chemical parameters

Surface energy is defined as the destruction of chemical bonds between molecules when creating the surface of a substance, which plays a crucial role on many surface-related phenomena (*3*). Based on the studies of M. Brajczewska, surface energy can be well related with EWF according to density parameter r_s (*57*). A certain relationship is established between these two parameters (*10*):

$$\gamma_i = \left(2 - \frac{\varphi_i}{\varphi_0}\right)\varphi_0 \tag{2.24}$$

where γ_i represents surface energy and φ_i represents EWF of specific crystal plane. φ_0 is the average EWF of all crystal faces in polycrystalline sample. It is clear that EWF and surface energy are highly dependent on crystal orientation (*58*), a crystal plane with higher EWF would generally have lower surface energy. For different materials, a higher EWF of material has a higher surface energy.

Adhesion is one of the applications on surface energy. As a manifestation of molecular force, adhesion refers to the mutual attraction of two different substances in contact. A higher surface energy can create larger adhesive force between counter faces, thus, a higher EWF could create higher adhesive force between phases. This mainly influences wearing and tribology process (*59*). Experimental data of EWF, friction and adhesion on 3d transition metals were presented in our research, which showed that adhesion and friction have certain correlation with EWF (*12*). Such relationship was also observed in austenite-ferrite duplex steel (*11*).

2.3 Experimental observations on correlations between EWF and properties of multi-elements solid solutions

Based on the ability of EWF to reflect atomic bond strength and electronic stability, relationships are established between EWF and intrinsic properties as shown in Chapter 2.2. Besides, experimental data of mechanical properties and EWF for pure metals was also given, which was in line with theoretical model. However, the relationships are established only for pure metals. Industrial materials are generally alloys with certain

microstructures. Thus, multi-elements alloys need to be investigated to understand the correlations between their properties and corresponding EWFs.

When two elements with different EWFs are mixed together, the overall EWF of alloy would change accordingly. Overall EWF could be well predicted if the material is in a solid-solution state (*60*). Based on Hao Lu's previous studies, Cu-Ni alloy with different Ni concentration were produced to clarify how overall EWF reflects properties of alloy (*15*). Lattice constants between Cu and Ni were assumed to be similar since Ni is homogeneously dissolved into Cu as an isomorphous solution. So overall EWF of alloy is approximately equal to:

$$\varphi_{AB}^{6} \approx X_A \varphi_A^6 + X_B \varphi_B^6 \tag{2.25}$$

where φ_A and φ_B are individual EWFs of metals, X_A and X_B are molar fraction of elements. EWFs of alloys calculated using the image model, first-principle method, and measured by UPS showed similar trends with different Ni concentrations. Red dots in figure 2.6 represent Cu-Ni alloys with different Ni concentration (*15, 61*). The relationship between Young's modulus and EWF of the isomorphous Cu-Ni alloy shows good fit with theoretical curve derived from pure metals. The overall EWF of the alloy increases with added Ni, which has higher EWF, corresponding to stronger atomic bonding between adjacent Cu-Ni bonds, and a higher barrier to any attempt to change the current mechanical state. Hardness of alloy also increases with increasing the overall EWF as shown in figure 2.9.

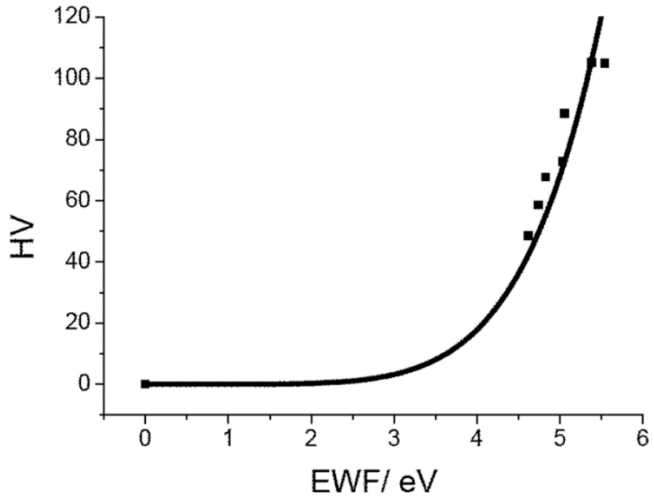

Figure 2.9 The fitted curve of hardness as a function of EWF on Cu-Ni alloy (*15*)

Sliding wear resistance was also related with EWF on Cu-Ni alloy (*16*). Based on Archard's equation (*62*):

$$WL = K_W \frac{F \times l}{H} \tag{2.26}$$

Wear volume loss (WL) is determined by wear coefficient (K_W), load (F), sliding distance (l) and hardness (H) of the sample. According to previous relation with EWF and hardness in Chapter 2.2.3.3, WL can be expressed as (*16*):

$$WL \propto \frac{F \times l(1-\upsilon^2)}{\varphi^6} \tag{2.27}$$

The wear volume loss has a reverse six-power relation with EWF, which represents wear resistance should increase with overall EWF. However, this depends on the wearing condition, experimental data could show sometimes an opposite trend, e.g., when formation and failure of oxide scales are involved (*16*). Besides, in the study of Cu-Ni

alloy, the corrosion behavior of Cu-Ni alloy was also measured in NaCl and HCl solutions respectively (*17*). Cu-Ni alloy dissolved without the formation of oxide layer in acid solutions. With higher overall EWF, a higher electrochemical stability is established corresponding to a more stable electronic state. In general, EWF can be used to predict properties of solid solution alloys.

2.4 Experimental observations on relations between EWF and properties of multiphases metallic materials

Previous researches have shown that EWF can be well correlated with properties of pure metals and isomorphous solid solutions. While most structural materials used in manufacturing have complex microstructure with multiphases, further studies are needed to determine whether EWF can be applied to multiphase materials. X70 steels adding by Ni were used to investigate the relationship between EWF and property (*63*). When a small amount of Ni (less than 10 wt. %) was added to the system, both EWF and mechanical properties increase because Ni has a higher EWF than iron and can bring in more "free" valence electrons to the system, leading to a higher stability on electronic state. With further increasing on Ni concentration, a second phase $FiNi_3$ was formed which has relatively lower EWF. The occurrence of $FiNi_3$ resulted in a lower overall EWF and deterioration on mechanical performance. However, the mechanisms regarding how the second phase influences the overall EWF is unclear.

For more information, SiC nanoparticle-reinforced Al matrix was used to analyze the overall EWF and corresponding corrosion resistance (*24*). As observed, EWF increased

with increasing the amount of SiC nanoparticles, along with higher corrosion potential and higher corrosion resistance. The valence electron density and electron localization function (ELF) were analyzed by first-principles calculations (*24*). As shown in figure 2.10C, the regions marked by arrows have higher values or ELF compared with other areas, which means more valence electrons are localized at the Al-SiC interfacial region. This indicates that interphase is a crucial factor and how the microstructure of multiphase materials mutually interact overall EWF needs to be determined.

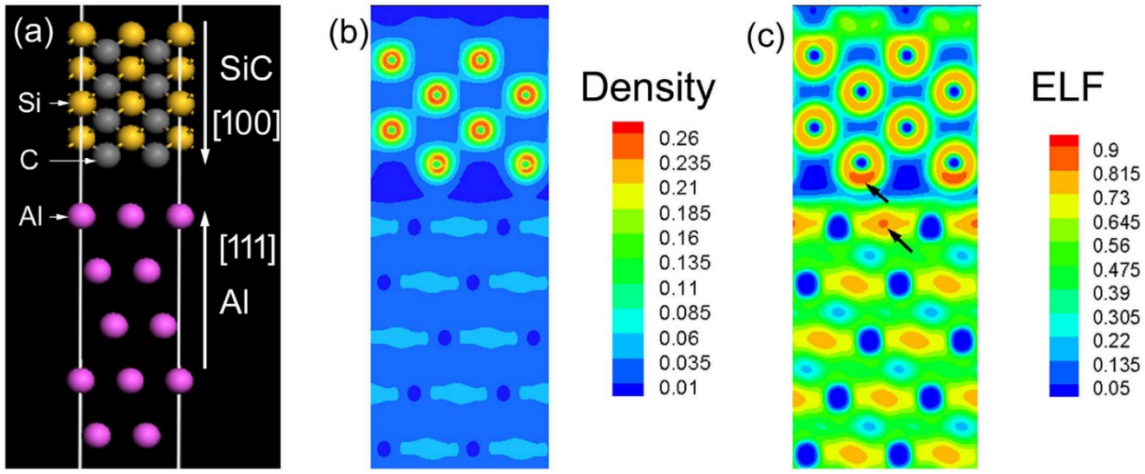

Figure 2.10 (a) The atomic configuration on Al-SiC interface, (b) Distribution diagram of valence electron density, (c) ELF of valence electrons (*24*)

2.5 Other applications of EWF

Since EWF is related to properties of metallic materials, it could be applied to various fields of material science. Below are a few application examples of EWF.

2.5.1 EWF as a probe for interfacial diagnosis

For multi-phases structural materials and composite materials, the interface plays a critical role in influencing their mechanical and chemical properties. However, how to evaluate the interfacial strength is challenging. EWF, which indicates electron behavior and atomic bond strength in material, could be used to diagnose the interphase condition by analyzing interfacial gradient of EWF. Conventional duplex stainless steels were used to study this phenomenon (*23*). As shown in figure 2.11, a steeper change of EWF at interface (point 2) resulted in a weaker interface with larger modulus and deformation magnitude. In general, a small interface gradient on EWF would create a stronger interface. Since EWF (φ) is directly related with electron density (ρ_e) (*7*), interfacial bonding is expected to correlate with electron density gradient:

$$\frac{d\varphi}{dx} \propto \frac{d}{dx\left(\rho_e^{1/6}\right)} \propto \frac{\rho_e^{5/6}}{6} \times \frac{d\rho_e}{dx} \tag{2.28}$$

A gradual change implies stronger interaction between the two phases in contact and thus stronger interfacial bonding. Theoretical calculation also proved that local EWF gradient should be used for evaluating interface rather than average one (*23*).

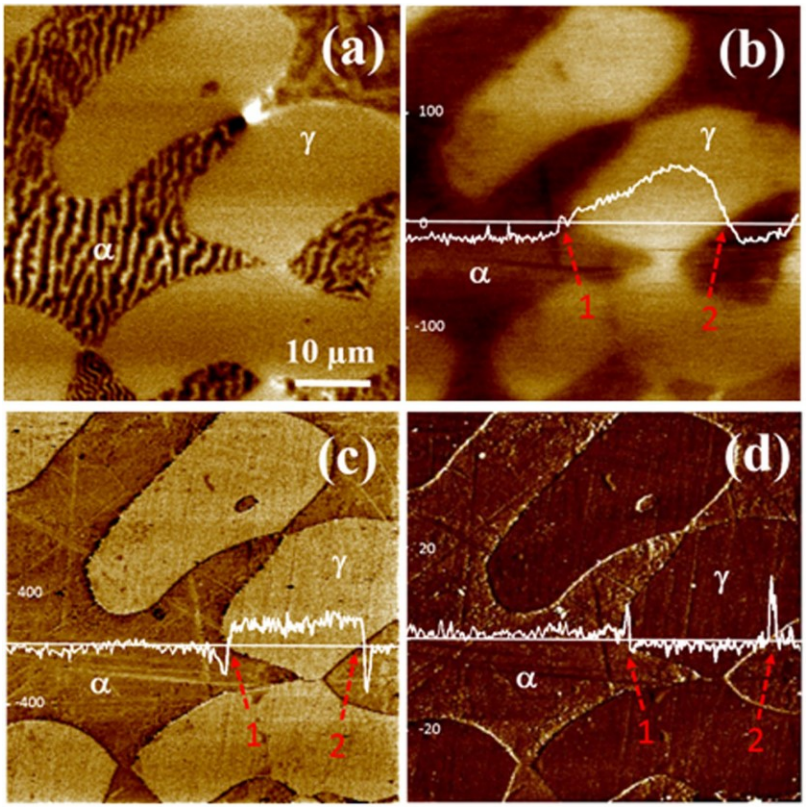

Figure 2.11 (a) Topography mapping of duplex stainless steel; (b) Work function mapping with interfacial gradient; (c) Modulus mapping with interfacial gradient; (d) Deformation mapping with interfacial gradient (*23*)

2.5.2 EWF-guided solute selection for enhanced solution hardening

EWF can be used as an indicator to select solute atoms for stronger solution hardening effect. Traditional mechanism for solution hardening contains elastic modulus and atomic size between solute and matrix (*64, 65*). Solution hardening can be related with atomic size misfit based on Mott and Nabarro's theory (*66*):

$$\delta_a = \frac{1}{a} \times \frac{da}{dc} \tag{2.29}$$

where a is lattice constant and c is solute concentration. Besides, modulus misfit between atoms can be expressed as (*65*):

$$\delta_G = \frac{1}{G} \times \frac{dG}{dc} \tag{2.30}$$

G is represented as shear modulus. However, how these two factors simultaneously affect hardening effectiveness is unclear, trial-and-error experiments are needed to select suitable solutes for effective solution hardening, which is time-consuming. EWF in here can be used as a bridge to connect atom size and elastic modulus, which has higher accuracy on predicting designed hardening effect. Hao Lu et al. derived the relationship between EWF and solution hardening effect (*67*):

$$F \approx |\kappa \Delta a + \tau \Delta G| = |[A(13.4\overline{\varphi} - 76.1) + B\overline{\varphi}^5]\Delta\varphi| \tag{2.31}$$

Where F is a parameter reflecting the hardening effectiveness, $\Delta\varphi$ is potential difference between the solute and host atoms and $\overline{\varphi}$ is average EWF, others are constant parameters based on host elements. It is clear that a higher EWF difference between host and solute atoms would increase solution hardening effect. Solutes with higher EWF would also increase average EWF with better solution strengthening. Cu-X alloys (adding by Ni, Zn, Ga) were used to verify this correlation and experimental observations are consistent with theoretical model (*67*). As shown in figure 2.12, Cu-Ni alloy with 20% Ni concentration presents highest hardness, due to the high value of $\Delta\varphi$ and $\overline{\varphi}$ in Cu-20%Ni alloy.

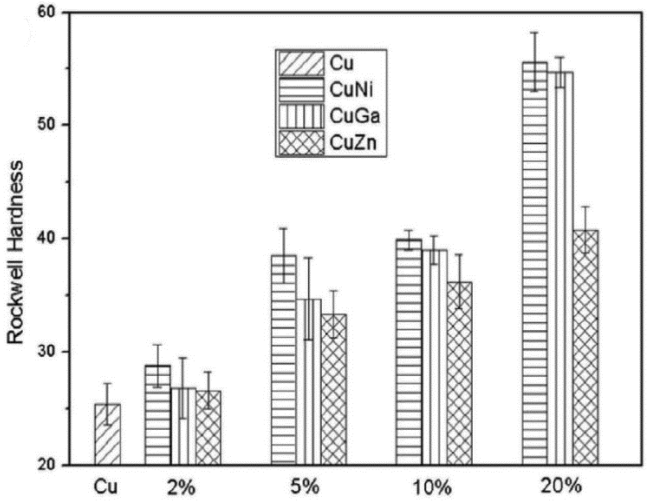

Figure 2.12 Hardness of Cu-X alloys with different concentration (*67*)

2.5.3 EWF in gas sensing purpose

Gas sensor has been widely applied in daily life and G-FET (gas sensing field effect transistors) is one of the most attractive technique in this field (*68*). The main challenge is to find applicable sensing material with good sensitive properties, high stability under extreme condition and compatible with matrix material. Since surface EWF of metal is expected to change based on interaction with gas atoms, EWF can respond to chemo-physical process, which is under electronic system by using sensing elements as conductors (*69*). Therefore, EWF can be well related with gas sensing technique as an approach to select potential sensing material. Alexandru Oprea gives a detailed development history on gas sensing technique based on application of EWF (*70*).

Chapter 3 Understanding the Microstructure – EWF – property relationship

Considerable studies have shown that EWF, the minimum energy required to move electrons from inside a metal at Fermi level to its surface (*7*), is related to Young's modulus and other mechanical properties of metals due to the fact that atomic bond strength is dependent on the electron state and has inherent correlation with EWF (*9, 23, 50, 71-75*). Both experimental and theoretical studies have shown that Young's modulus and intrinsic hardness of metals exhibit six-power relationships with EWF (*7, 8*). The mechanical strength is affected by the electron state. A higher EWF represents a more stable electronic state, thus a higher resistance to mechanical deformation. As shown in Chapter 2.3, adding Ni ($\varphi_{Ni} = 5.1$ eV) to Cu ($\varphi_{Cu} = 4.6$ eV) forms a solid solution having elevated overall EWF and Young's modulus since Ni brings in more free electrons to the system (*15*) and EWF is dependent on the electron density. However, how EWF affects mechanical properties of multiphase materials is unclear. This hinders the application of EWF in realistic material design. Structural materials generally have multiphase microstructures (*19, 20*), which influence the mechanical properties due to their dependence on grain size, 2nd phases, and other microstructural factors (*21*). Microstructural factors mutually interact and the overall properties are integrated from those of individual microstructural constituents in the material. Although properties of individual phases are related to their EWFs, whether the overall EWF of a multiphase material reflects its integrated electron behavior and overall properties is unclear. It is thus of significance to determine how the microstructure affects the overall EWF and corresponding properties of multiphase

materials, towards the design of materials on a feasible electronic base or through "electronic metallurgy".

When two phases having different EWFs are in contact, electrons move from the low-EWF phase to that having a higher EWF, forming a dipole layer at the interface which stops continuous electron movement (*23*). The above process would lead to redistribution of charges between phases, thus affecting the apparent work function of the system. It is expected that the apparent EWF can reflect overall properties of the system. To confirm this, we investigated microstructure - EWF - property relationships using high-Cr cast irons (HCCI: 40 wt.% Cr with 1-6 wt.% C) as a sample material. Results of the study are reported in this Chapter.

3.1 Experimental procedure

3.1.1 Sample preparation

Materials used for the study were high-Cr cast irons with compositions of 40 wt.% Cr, 1-6 wt.% C, balanced by iron and minor elements (2.2-2.8 wt.% Mn and 0.8-1.4 wt.% Si etc.). Samples were made using an arc furnace and cast in a mold. After modeling, the samples were treated at 950 ℃ for 5 hours and then slowly cooled to room temperature. The samples were polished using sand papers up to 1200 grit, and then polished by using 1μm diamond slurry. Chemical etching was used to remove oxide layer and distinguish different phase features, followed by ultrasonic cleaning in ethanol and dried with a compressed gas flow.

3.1.2 Experimental details

Samples were cut to 50mm×10mm×5mm dimension to measure Young's modulus using an acoustic instrument with RFDA basic software (IMCE company) for data analysis. Operating device is shown in figure 3.1. Sample is mechanically tapped by a flexible hammer and the induced vibration signal is detected by microphone above the sample. Elastic properties can be calculated based on the dimensions of the sample and other detected data. Microstructure were analyzed using a Hitachi S-2700 scanning electron microscope equipped with an ultrathin window X-ray detector. Samples of 10mm×10mm×5mm in dimensions were used for EWF analysis. A scanning Kelvin Probe (KP Technology, UK) was employed to measure work functions of the samples. Bruker Multimode AFM8 with PeakForce KPFM capability was used to measure the local work function. Bruker magnetic probes were used for work function measurement, and diamond probes with 350 N/m force constant were used to determine modulus and deformation. The AFM in situ mapping was used to distinguish the difference in properties between carbide and matrix. Image-Pro Plus 6.0 was adopted to analyze interfacial area/volume of matrix. To keep the data accurate, graphs were cut from optical microscopes with exactly same pixels on six samples. The system was set under "Std. Optical Density" mode and before every counting, the unit was transformed from pixel to micron in scaling calibration. All the parameters were consistent during the whole counting process between six samples.

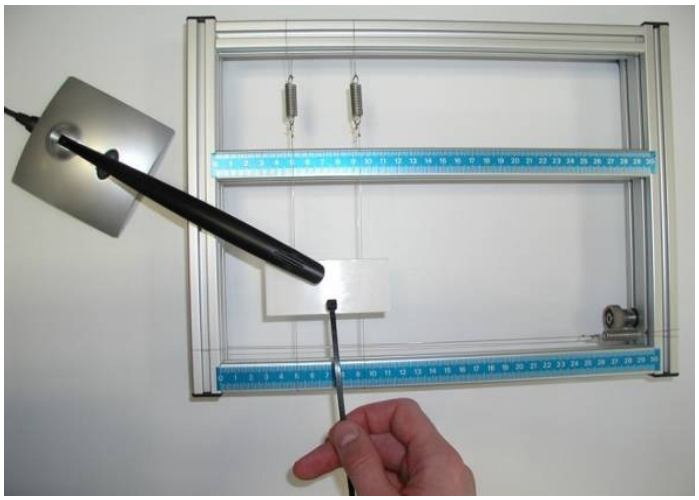

Figure 3.1 Acoustic instrument for measuring Young's modulus

3.1.3 Computational details

First-principles calculations were conducted based on the density functional theory (*76*) (DFT) using Vienna ab-initio simulation package (VASP) (*77-79*). Electron interactions were treated with the projector-augmented wave method. The generalized gradient approximation (GGA) of Perdew-Burke-Ernzerhof (PBE) was adopted for the exchange and correlation potentials (*80*). Cut-off energy of 450 eV and 3×3×1 k-point mesh (*81*) was used for all calculations. Energy difference of 10^{-5} eV was set as the convergence condition for self-consistency calculations, and geometry relaxation tolerances were 10^{-2} eV/Å for force and 10^{-5} eV for energy. The interface models were constructed by contact between (001) surface of carbide ($Fe_4Cr_3C_3$) and (110) surface of iron. The boundary was periodic in the interface plane. A vacuum layer of 15 Å was built along the direction perpendicular to the plan of interface, and the energy for an election moving from surface of iron to vacuum was calculated as EWF of the system. The EWF

was defined by the difference between the vacuum potential and the Fermi energy. This work is done in collaboration with Dr. Yunqing Tang.

3.2 Results and discussion

3.2.1 Phases and microstructures of various samples

Depending on the carbon concentration, the HCCI consisted eutectic $M_{23}C_6$ carbides and primary M_7C_3 carbides. When the carbon content is within 1% and 2%, fine $M_{23}C_6$ carbides are present. Within 3%C - 4%C, $M_{23}C_6$ and M_7C_3 carbides co-exist. After 4%C, only M_7C_3 primary carbide show up (*82*). Compared to the ferrous matrix, M_7C_3 and $M_{23}C_6$ show almost the same local work function measured using AFM mapping (Chapter 3.2.3). To highlight core factors, this study focused on the effects of size, fraction and special arrangement of the carbides on EWF and overall properties of the material.

Scanning electron microscopy images (figure 3.2) show microstructural characteristics of samples. This alloy system consists of carbides (dark) and the metallic matrix (grey) with red interfacial line. With increasing the carbon content from 1 wt.% to 2 wt.%, the fraction of carbides increases considerably, accompanied with an increase in the carbide/matrix interfacial area. As the carbon content continuously increases, primary carbides occur and the total interfacial area decreases. Further increasing the carbon content to 6 wt.%, the primary carbide becomes predominant with further decrease in the total interfacial area.

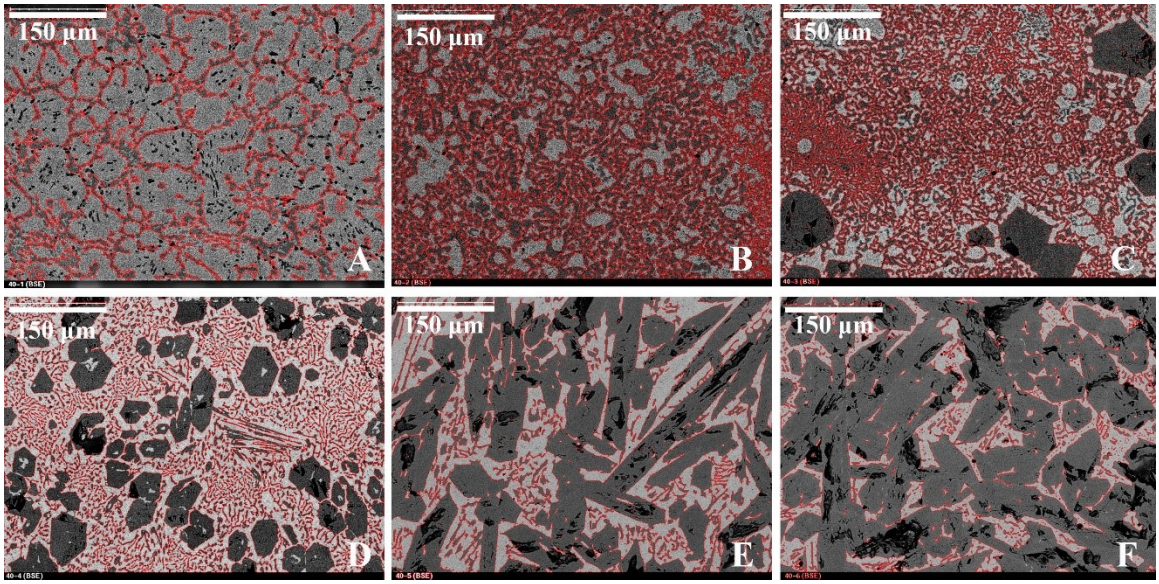

Figure 3.2 SEM images with interfacial lines: (A) 40 wt.% Cr - 1 wt.% C, (B) 40 wt.% Cr - 2 wt.% C, (C) 40 wt.% Cr - 3 wt.% C, (D) 40 wt.% Cr - 4 wt.% C, (E) 40 wt.% Cr - 5 wt.% C, (F) 40 wt.% Cr - 6 wt.% C

3.2.2 Relationship between Young's modulus and overall EWF

Figure 3.3 illustrates overall EWF (measured using Kelvin Probe technique) and Young's modulus (measured by acoustic measurement) versus the carbon content. As shown, both of the properties increase synchronously, reaching maximum values at 2% C, and then decrease with further increasing the carbon content. The coincident changes in the two properties with microstructure are of significance to the application of EWF as a guiding parameter in material design, similar to the situations of metals and single-phase solid solutions (*15*). Table 3.1 gives experimental data of properties on 40% Cr series HCCI.

Table 3.1 Overall Young's modulus and EWFs of different samples

Sample	1%C	2%C	3%C	4%C	5%C	6%C
E (GPa)	233.62	263.35	261.20	227.42	171.79	120.05
EWF (eV)	4.59	4.76	4.60	4.55	4.54	4.36

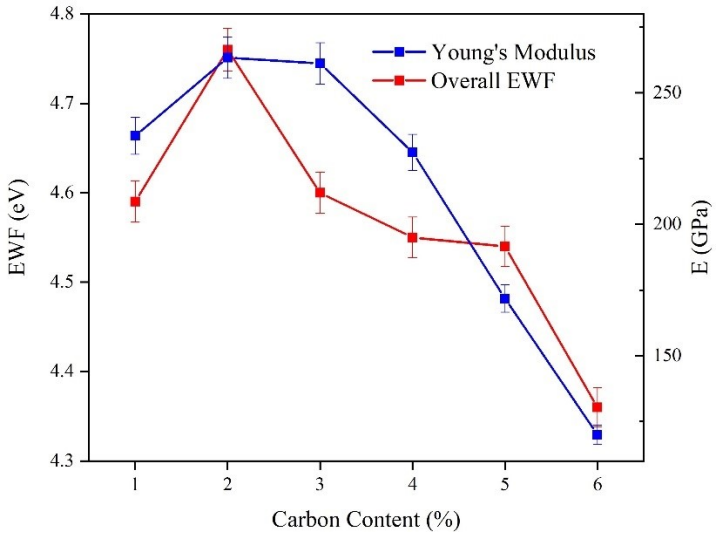

Figure 3.3 Overall EWF vs Young's Modulus of samples with different carbon contents

3.2.3 Local EWF differentiation between samples

To obtain further information on the relation between the overall EWF and those of individual phases, we employed AFM to analyze local properties of Fe-40%Cr-5%C HCCI as a sample material. Figure 3.4A is a topography image showing carbide (light) and matrix (dark), and figures 3.4(B-D) illustrate corresponding EWF, modulus, and deformation maps. Figure 3.4F shows variations in potential or EWF measured along a line marked in figure 3.4B. Carbides have higher EWFs than the matrix, and the eutectic $M_{23}C_6$

has its EWF slightly lower than that of M_7C_3 (as figures 3.4B and F). These maps further confirm the coincident variations in EWF, modulus and deformation versus the carbon content.

Figure 3.5 represented other work function mapping except for 5% carbon content. According to the AFM analysis for 40Cr-2C, 40Cr-3C and 40Cr-4C samples, primary carbide and eutectic carbide have similar electron work functions. Thus, we mainly focus on microstructure difference between the carbides and the matrix.

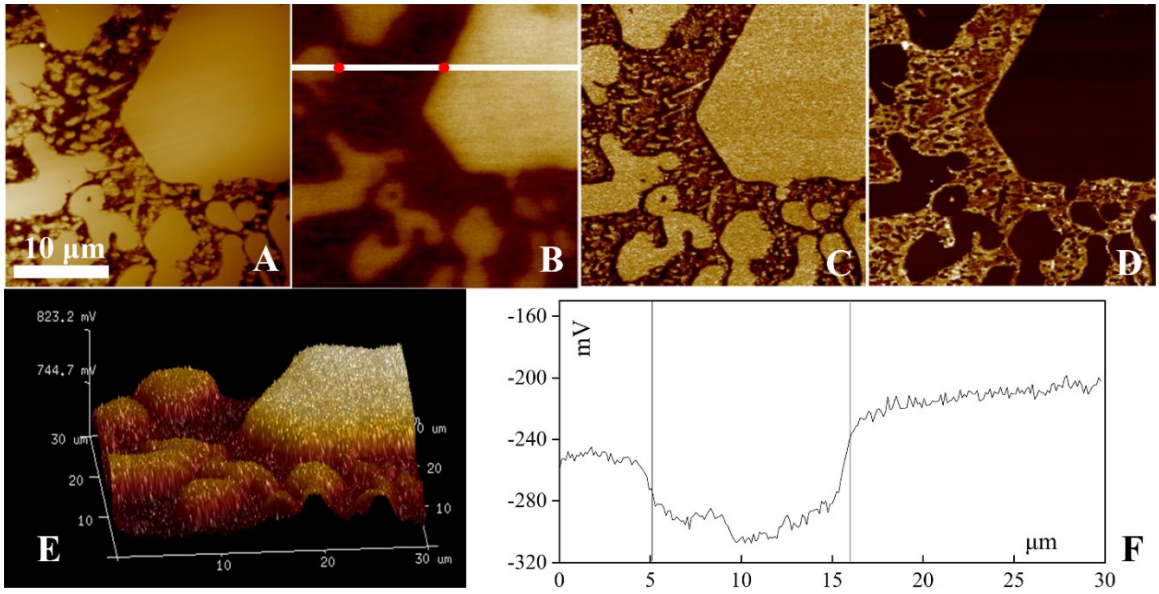

Figure 3.4 AFM mapping with 40%Cr - 5%C sample: (A) Topography, (B) Work function, (C) Modulus, (D) Deformation, (E) A 3D image showing potential difference, (F) Profile of EWF along the line shown in B

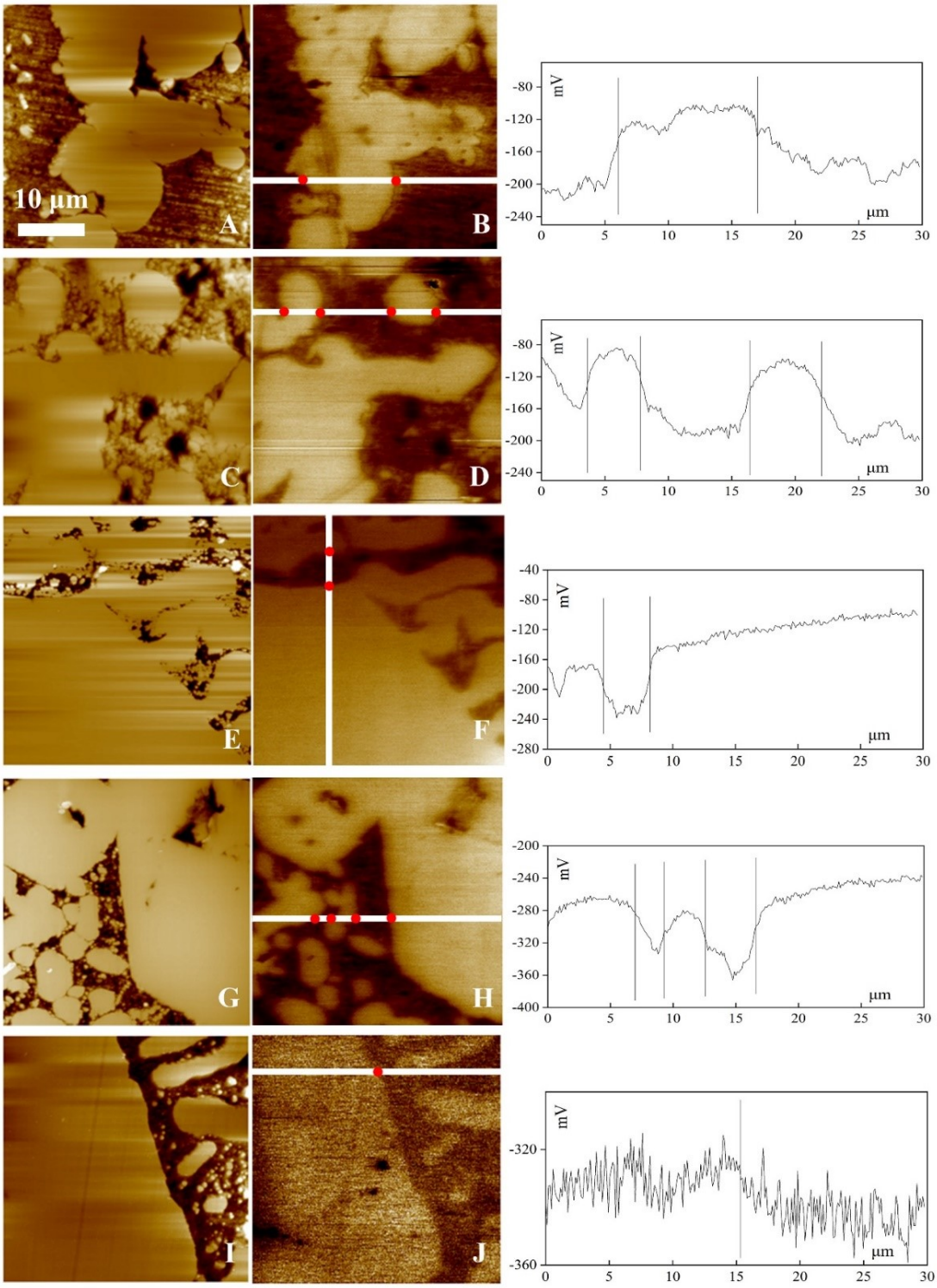

Figure 3.5 AFM maps of Fe-40 wt.%Cr-1 wt.%C sample: (A) Topography, (B) Work function; Fe-40 wt.%Cr-2 wt.%C sample: (C) Topography, (D) Work function; 40

wt.%Cr-3 wt.%C sample: (E) Topography, (F) Work function; Fe-40 wt.%Cr-4 wt.%C: (G) Topography, (H) Work function; Fe-40 wt.%Cr-6 wt.%C sample: (I) Topography, (J) Work function. The line profile on the right side shows potential difference between carbide and matrix.

It is noticed that the samples with further higher fractions of primary carbides, e.g., Fe-40%Cr-6%C, showed lowered overall EWF and Young's modulus. Figure 3.6 illustrates EWFs of carbide and matrix with different C concentration. The variations in EWF of the samples are consistent with those measured using the Kelvin Probe. At 2%C, EWF shows the highest value and then decreases with increasing the carbon content. The average potential difference between carbide and matrix is about 0.1 eV when the carbon content is in the range of 2%~3%. This difference decreases with increasing the volume fraction of carbide, and EWFs of carbides and the matrix approach each other at 6%C. Such changes are an indication that the work functions of the carbide and matrix affect each other and synergistically influence the overall Young's modulus.

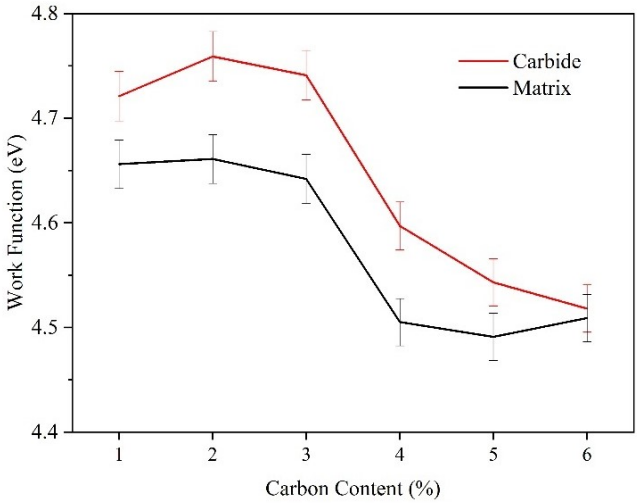

Figure 3.6 Local potential difference between samples

3.2.4 Understanding the observed relationships with a proposed charge compensation model

EWFs of carbide and matrix may mutually influence each other through the following mechanism. When carbide and matrix are in contact, as φ (carbide) >φ (matrix), electrons move from the matrix to the carbide until a dipole layer is established at their interface, which balances the potential difference and stops further electron movement. As illustrated in figure 3.7A, the driving force for the electron movement is the potential difference and the established double layer compensates the potential difference, thus preventing the further movement of electrons (*23*). Such electron movement makes electrons depleted inside the matrix and thus renders the matrix electrically positive, which increases the difficulty for electrons to escape from the matrix, leading to an elevated apparent EWF. Such a change in EWF may be termed as a charge-compensation phenomenon, which is dependent on the amount of carbides, the carbide/matrix interfacial area, and the spacing between adjacent carbides. Thus, the measured EWF should carry the information about the microstructural influence on the overall electron behavior.

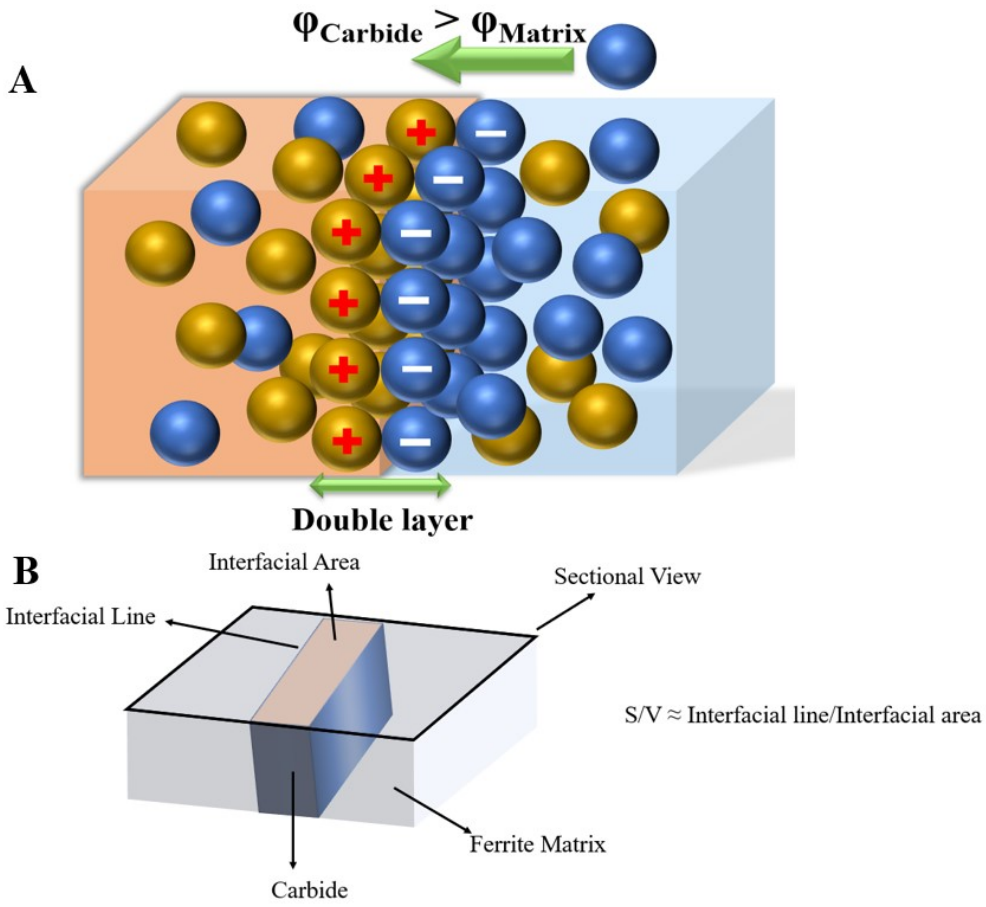

Figure 3.7 (A) Interfacial dipole layer between carbide and the matrix, (B) 3D schematic of alloy

Let's look at a carbide/matrix interface, considering an interface between carbide and matrix having an area of S, where an electrical diploe layer forms with the interfacial charge density of σ, resulting from the contact potential due to the difference in work function between the two phases. The formed diploe layer establishes an opposite electrical filed, blocking further electron migration from the low-EWF matrix to the high-EWF carbide. Assume that the matrix has a volume of V_m and its free electron density equals ρ_{e-} , the change in the free electron density of the matrix, $\Delta\rho_{e-}$, is related to the interfacial charge at the dipole layer,

$$V_m \cdot \Delta\rho_{e-} = S \cdot \sigma \tag{3.1}$$

Based on previous studies, the initial work function of the metallic matrix without being in contact with the carbide is dependent on the electron density (*7*):

$$\varphi_{initial} = \alpha\rho_{e-}^{\frac{1}{6}} \tag{3.2}$$

$$\alpha = \frac{e^3 m^{\frac{1}{2}}}{16^3\sqrt{3}\pi^{\frac{5}{3}}\hbar\varepsilon_0^{\frac{3}{2}}} \tag{3.3}$$

where $\hbar$ is Planck's constant, m is mass of electron and ε_0 is vacuum permittivity. When carbide with higher EWF is in contact with the matrix, the change in work function of the matrix is expressed as:

$$\Delta\varphi = \alpha\frac{1}{6}\rho_{e-}^{-\frac{5}{6}}\Delta\rho_{e-} \tag{3.4}$$

During overall EWF measurement, electrons escape from weaker locations on sample surface with lower local EWFs. Thus, the percentage change of the overall work function is related to the EWF of the matrix as a function of interfacial area, interfacial charge density, volume of matrix, and variation in its free electron density:

$$\frac{\Delta\varphi}{\varphi_{initial}} = \frac{\Delta\rho_{e-}}{6\rho_{e-}} = \frac{S\sigma}{6V_m\rho_{e-}} \tag{3.5}$$

According to Poisson's equation on electrostatics (*83, 84*):

$$\nabla^2(V) = \frac{d^2V}{dx^2} = -\frac{\rho_{int}}{\varepsilon_0} \tag{3.6}$$

where V is the contact potential at the carbide/matrix interface, the interfacial electron density ρ_{int} (Coulomb) is equal to:

$$\rho_{int} = \sigma e \tag{3.7}$$

σ is the interfacial charge density (unit is 1), e is the unit charge:

$$\Delta\varphi\ (eV) = \varphi\ (carbide) - \ \varphi\ (matrix) \tag{3.8}$$

Thus, we have

$$\frac{d^2(\Delta\varphi)}{dx^2} = \frac{\sigma e^2}{\varepsilon_0} \tag{3.9}$$

Thus, we get the expression of interfacial charge density:

$$\sigma = \frac{2\varepsilon_0 \Delta\varphi}{x^2 e^2} \tag{3.10}$$

where ε_0 is vacuum permittivity, and x is half the width of the dipole layer. According to equation (3.10), the interfacial charge density is proportional to the potential difference or the difference in work function between the two phases in contact. The typical width of doped p-n junction depletion layer is 10^2~10^3 Å (*85*) and the higher doping density, the lower depletion layer width. To simplify the analysis without losing physical significance, we assume x=100Å as cast iron had higher free electron density. $\Delta\varphi$ was determined through AFM mapping (figure 3.6). Based on the obtained experimental data, the interfacial charge density can be calculated and details are provided in table 3.2. Since the overall work function is directly related to S/V ratio, for comparison purpose, the length of interfacial line over the cross-section area of ferrite phase roughly equals to the S/V ratio

(figure 3.7B). As shown in figure 3.8, S/V ratio reaches the maximum at 2%C and then decreases. The free electron density ρ_{e-} can be replaced by density parameter r_s (*52*) which is determined by atomic related parameters:

$$\rho_{e-} = \frac{3}{4\pi r_s^3} \tag{3.11}$$

where r_s for Fe is 1.04 Å, r_s for Cr is 1.05 Å (*52*). Thus, the initial matrix's free electron density is determined as 2.12×10^{29} electrons/m^3. With the above data, the percentage increase in work function can also be calculated, results of which are shown in figure 3.9. The improvement of overall work function reaches 4.25% at 2% carbon content, which has the highest S/V ratio with fine carbide microstructure. From accepted work function calculated by electron density (*52*), work functions of Fe and Cr are at the same level of 4.5 eV, thus, $\varphi_{initial}$=4.5 eV was used in the calculation. Figure 3.10 gives comparison between theoretical and experimental overall EWFs, the similar trends indicate that this model works well for multiphase materials. Detailed data (e.g., local work function, interfacial and matrix area, etc.) used in model calculations are given in Table 3.2.

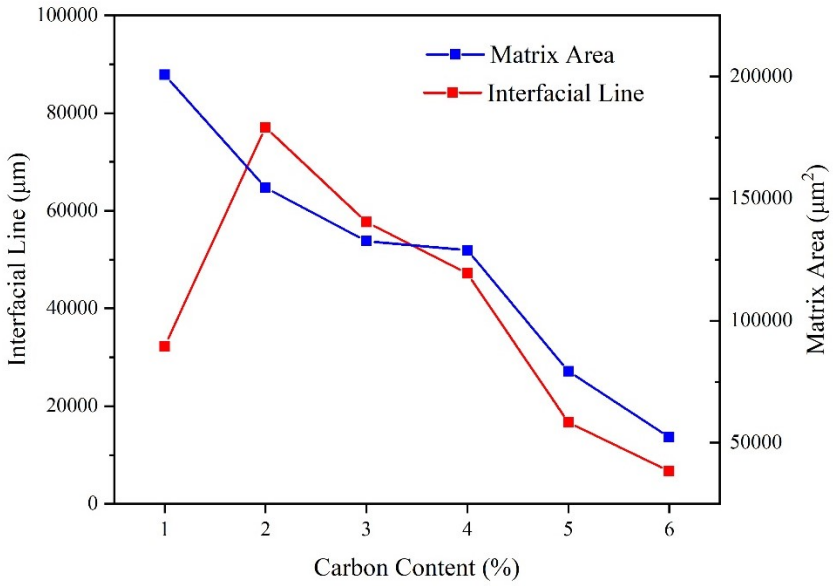

Figure 3.8 Value of interfacial line and matrix area

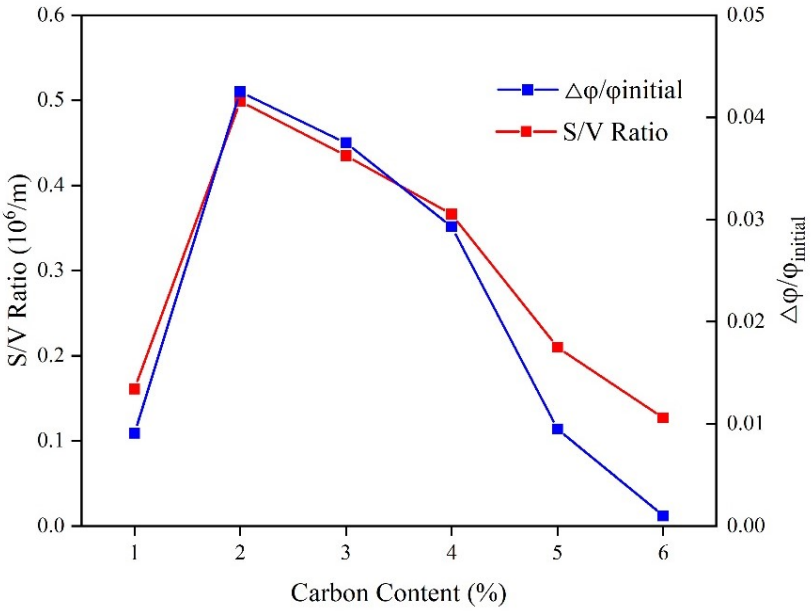

Figure 3.9 Ratio of S/V and $\Delta\varphi/\varphi_{\text{initial}}$

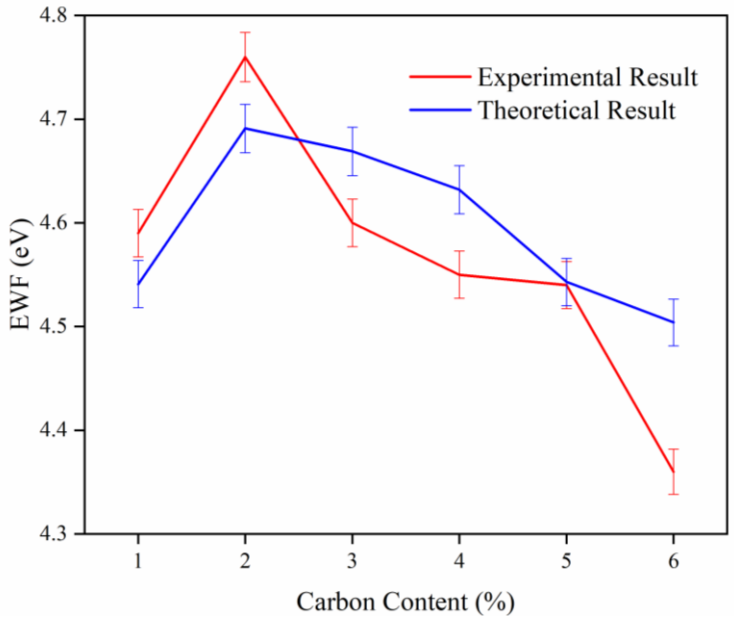

Figure 3.10 Comparison between theoretical and experimental results

Table 3.2 Detailed data (e.g., local work function, interfacial and matrix area, etc.) used in model calculations

Carbon %	1	2	3	4	5	6
$\varphi_{carbide}$ (eV)	4.721	4.759	4.741	4.597	4.543	4.518
φ_{matrix} (eV)	4.656	4.661	4.642	4.505	4.491	4.509
$\triangle\varphi$ (eV)	0.065	0.098	0.099	0.092	0.052	0.009
interfacial line (μm)	32297	77057	57681	47147	16638	6665
carbide area (μm^2)	65850	112724	135176	138490	185798	213198

Percentage of carbide (%)	0.247	0.422	0.505	0.518	0.701	0.803
Matrix area (μm^2)	200749	154395	132499	128865	79249	52304
S/V (10^6/m)	0.161	0.499	0.435	0.366	0.210	0.127
$\triangle\varphi/\varphi_{initial}$ (%)	0.91	4.25	3.75	2.93	0.95	0.10
$\varphi_{theoretical}$ (eV)	4.541	4.691	4.669	4.632	4.543	4.504

3.2.5 Further verification of the model through first-principles calculations

As demonstrated, the overall EWF carries the information about the microstructural influence on the overall electron behavior. This has also been confirmed by first-principles calculations. Figure 3.11 illustrates three interfacial model systems having iron in junction with carbides having different spacings between adjacent carbides. The systems have $(001)_{(Fe_4Cr_3)C_3}$ // $(110)_{Fe}$ interfaces. The energy for taking an election from surface of iron to vacuum was calculated as EWF of the system. As shown, the work function increases when the distribution of carbides becomes denser with smaller spacing between adjacent carbides, which contributes to a higher S/V ratio of the system.

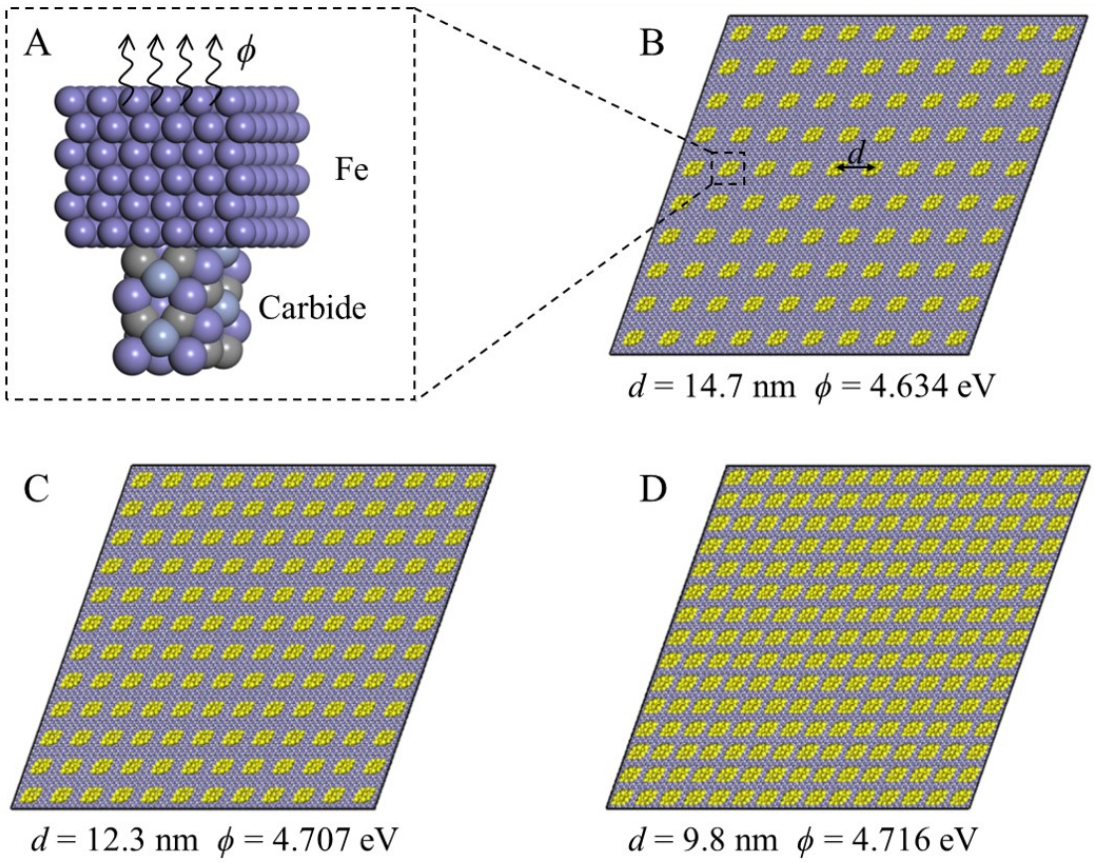

Figure 3.11 Schematic diagrams and EWFs of three interfacial configurations. (A) a model of carbide/Fe interface; the calculated EWF is the energy for electrons to escape from the surface of iron. (B) - (D) EWFs of models with different spacings between adjacent carbides

3.3 Conclusions

In summary, using high-Cr cast irons as a sample material, we demonstrate that the apparent EWF of the multiphase alloy reflects the integrated electron behavior and overall properties. Both EWF and Young's modulus increase synchronously, reaching maximum values with 40 wt.% Cr - 2 wt.% C sample. When two phases having different EWFs are in contact, a dipole layer forms at the interface, leading to depletion of electrons in the low-

EWF phase and thus rendering it more positive. This charge-compensation process increases the overall EWF, which is affected by the microstructural arrangement. The study demonstrates that the overall EWF does reflect the overall properties of multiphase materials. Establishing the relationship is a crucial step towards design of structural materials through “electronic metallurgy”.

Chapter 4 Microstructure – EWF – property relationships in low carbon steel having two levels of microstructural inhomogeneity

Attributed to the intrinsic correlation between EWF and the atomic bond strength and electronic stability, which govern mechanical and electrochemical properties of materials, EWF has been successfully applied to material analysis and design. Chapter 3 reports a study on the relationship among microstructure, EWF and property, based on a simple multiphases system. In this chapter, this model is further verified with a study on low carbon steel with higher microstructural complexity, which is widely used in manufacturing. By adjusting the cooling rate of heat treatment, the size and distribution of pearlite and cementite can be well controlled, and the steel shows two levels of microstructure inhomogeneity. The low carbon steel experiencing annealing and cooling in furnace (LCA) contains coarse pearlite and ferrite matrix with large grain size, while the low carbon steel under normalizing condition (LCN) shows relatively fine pearlite in the ferrite matrix when cooled at a higher cooling rate. Microstructure and property differentiation between LCA and LCN are connected using EWF as a bridge, which indicates that EWF can also be used to guide multiphase metallic material design. The proposed charge-compensation model works well for the present case as well.

4.1 Experimental procedure

4.1.1 Sample preparation

ASTM A109 carbon steel was used for the study, which contains 0.13-0.20 wt.% C, 0.30-0.90 wt.% Mn, max. 0.04 wt.% P, 0.15-0.30 wt.% Si, and max. 0.50 wt.% S, balanced by iron. Samples were annealed in a tube furnace at 760 ℃ with argon atmosphere for 1 hour. The LCA samples were cooled in the furnace with a 50℃/h cooling rate and LCN samples were cooled in air. After the heat treatments, samples were cut and polished using SiC abrasive papers of 180, 320, 400, 800, 1200 grit successively, and then polished using 1μm diamond slurry. A 2% nital solution was used as the etchant to remove a deformed layer and distinguish pearlite from ferrite, followed by ultrasonic cleaning in ethanol for 5 min and dried with a compressed air flow.

4.1.2 Experimental details

Optical micrographs (Mitutoyo Finescope, FS60), Scanning Electron Microscope (SEM, CamScan MV2300, UK) and Transmission Electron Microscope (TEM, a Hitachi H-7000) were used to analyze microstructure differences. Phase differences were analyzed by X-ray Diffraction (XRD, Rigaku Ultima IV with Cobalt tube at 38kV and 38mA), scanning range was from 25° to 100° and scanning speed was 2 deg/min. JADE 9.6 software was used to analyze phase information. Samples were cut to 30mm × 6mm × 3mm dimension to measure Young's modulus using an acoustic instrument with RFDA basic software (IMCE company) for data analysis. Hardness was measured by Indentec Hardness Testing Machine based on Vickers hardness. At least five measurements were carried out

on each test. Electrochemical experiments were conducted at room temperature based on Gamry electrochemical workstation. 3.5 wt.% NaCl solution and 0.5 mol/L HCl acid solution were used to measure corrosion resistance. The saturated calomel electrode (SCE) was reference electrode and Pt plate was used as counter electrode with 1 cm^2 area. Scan rate was set to be 0.33 mV/s. Samples in dimension of 10mm × 10mm × 5mm were used for EWF analysis. A scanning Kelvin Probe (KP Technology, Caithness, UK) with a gold tip was employed to measure overall work functions of the samples. Bruker Multimode Atomic Force Microscope8 (AFM) with PeakForce KPFM capability was used to measure the local work function with Bruker magnetic probe. The potential difference between pearlite and matrix was distinguished by using AFM in situ mapping. Interfacial area/volume of matrix simulation was analyzed by Image-Pro Plus 6.0. To keep the data accurate, graphs were cut from optical microscopes with exactly same pixels between LCA and LCN samples. The system was set under "Std. Optical Density" mode and before every counting, the unit was transformed from pixel to micron in scaling calibration. All the parameters were consistent with LCA and LCN counting processes.

4.2 Results and discussion

4.2.1 Microstructure differentiation under different cooling conditions

Figure 4.1 shows XRD patterns of the LCA and LCN samples. Comparing with standard powder diffraction patterns, it is shown that Fe (01-087-0721) and Fe_3C (03-065-2412) are present in the samples without existence of other phases. Based on the

microstructure observations and XRD analysis, the furnace cooling and air cooling did not result in changes in phase constituents but affected the degree of microstructural coarsening.

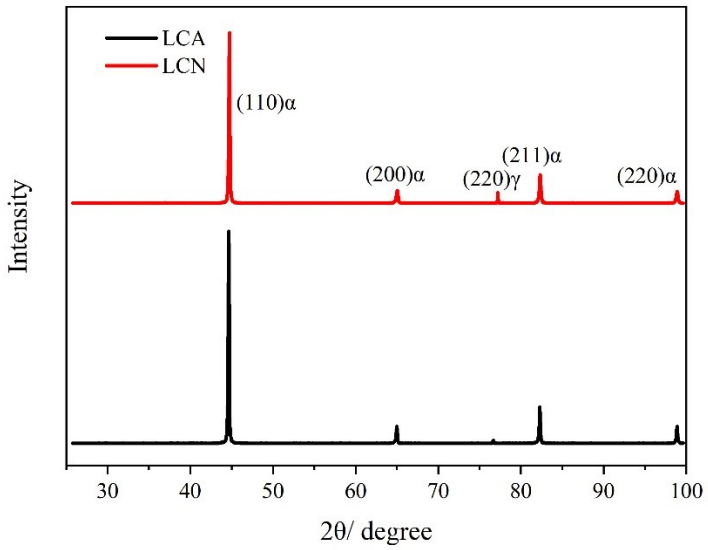

Figure 4.1 XRD patterns of LCA and LCN samples

Representative optical, SEM and TEM images of the low-carbon steel are presented in figure 4.2. A coarse pearlite microstructure of the LCA sample having its average grain size of 100μm is illustrated in figures 4.2 (A-G). With relatively lower cooling rate, austenite has enough time to transform into coarse pearlite (*86*). In contrast, the LCN sample shows fine pearlite (average grain size is around 20μm) with more densely distributed cementite in the pearlite domains, as figures 4.2 (H-N) illustrate. With similar volume fraction of pearlite, LCN sample shows higher interfacial area between pearlite and iron matrix. Figure 4.2 (D, E) and (K, L) show SEM backscattered images of LCA and LCN sample, respectively. A lamellar microstructure is observed in pearlite with composition of plate cementite and iron matrix. TEM images of pearlite between two samples are presented in figure 4.2 (F, G, M, N) to understand microstructure difference in

pearlite. LCN sample has finer and denser plate-like cementite, compared to the LCA, corresponding to a larger total interfacial area between ferrite and cementite, proving that the cooling rate does not only affect the size and distribution of pearlite, but also distribution and thickness of cementite in pearlite. Having a finer microstructure with higher interfacial area leads to higher overall work function, thus, a more stable electronic state is established under physical and electrochemical attack.

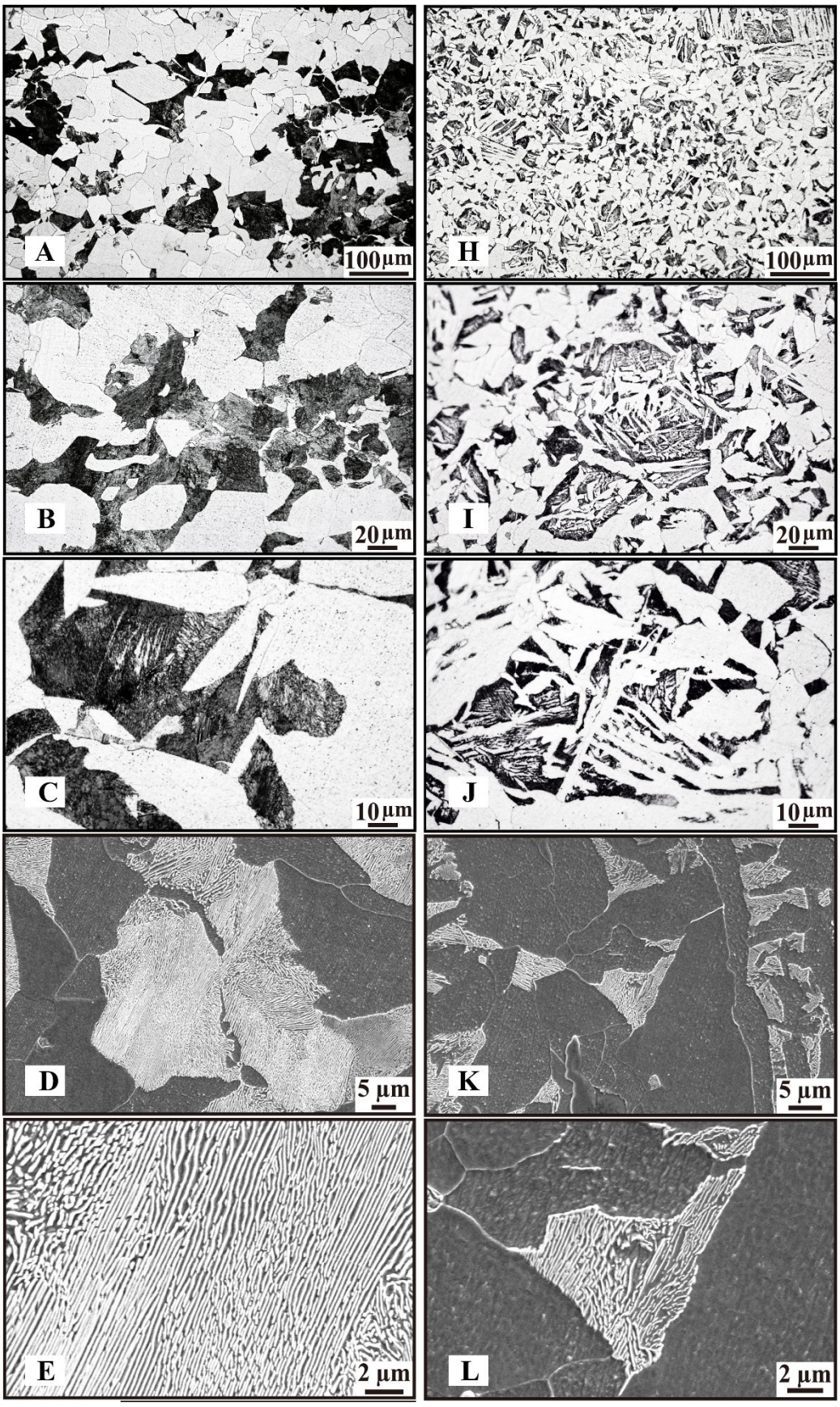
A
100μm
H
100μm
B
20μm
I
20μm
C
10μm
J
10μm
D
5 μm
K
5 μm
E
2 μm
L
2 μm

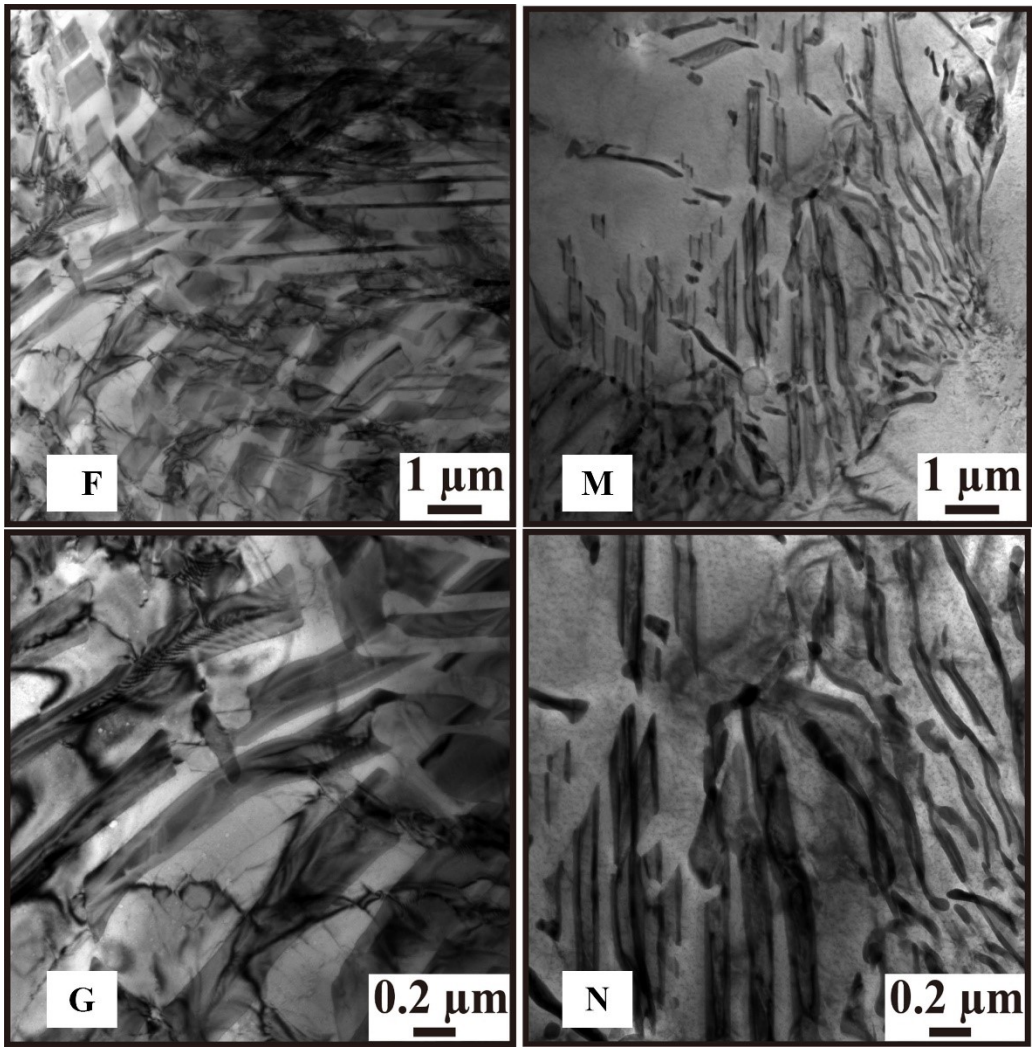

Figure 4.2 (A - C) Optical micrographs of LCA, dark regions are pearlite and white regions are ferrite matrix; (D, E) SEM images of LCA; (F, G) TEM images of pearlite in LCA; (H - J) Optical micrographs of LCN; (K, L) SEM images of LCN; (M, N) TEM images of pearlite in LCN

4.2.2 Relationship between mechanical performance and EWF

Young's moduli, hardness values and overall work functions of the low-carbon steel were measured. The mechanical properties versus EWF are illustrated in figure 4.3.

Both Young's modulus and hardness of the normalized sample show higher values, corresponding to its higher EWF. Table 4.1 gives the measured values of the properties. The results are consistent with previous observations that the trend of changes in mechanical property is similar to that of corresponding changes in electron work function (*25, 63, 87*). The value of overall EWF represents the stability of valence electron and bond strength between atoms. LCN sample has finer pearlite microstructure with a larger total interfacial area, leading to a stronger electron redistribution effect and a higher overall EWF, which corresponds with a higher atomic bond strength. As an intrinsic property, Young's modulus is directly related to the atomic bond strength of material. The higher Young's modulus of the LCN sample and correspondingly higher EWF imply that the overall mechanical strength and the apparent EWF of a two-phase alloy should be correlated in a certain way. Electrons must be redistributed in order to reflect the changes in the overall properties that integrate contributions from various phases with certain microstructural features. Such electron redistribution lead to the development of a certain relationship between the mechanical properties and EWF, which may be similar to those for pure metals and homogeneous solid solutions. As shown in figure 4.3, the change in hardness is similar to that of Young's modulus. Although hardness is less intrinsic, a higher EWF corresponds to stronger atomic bonding and a higher resistance to plastic deformation involving dislocation generation and movement (*8, 67*). As a result, both hardness and Young's modulus show higher performance with increasing overall EWF in low carbon steel, indicating that multiphase materials still follow the EWF – property relationship.

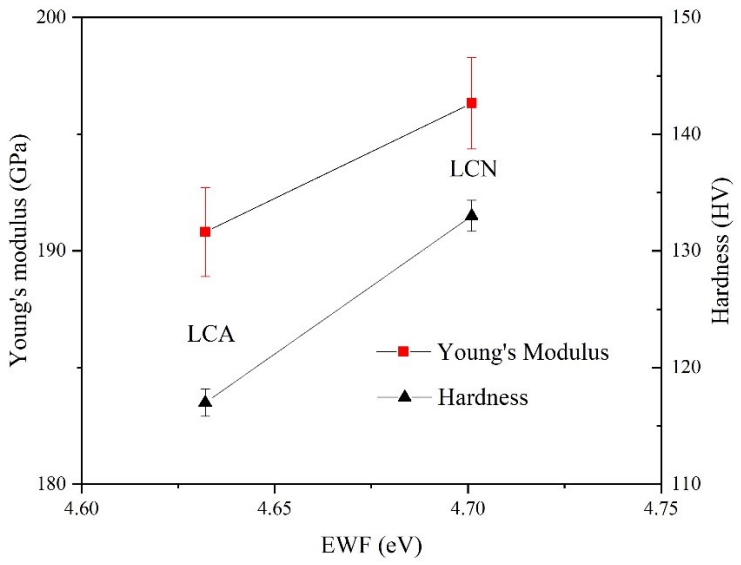

Figure 4.3 Relationship between mechanical property and overall EWF

Table 4.1 Overall properties of LCA and LCN samples

	Young's Modulus (GPa)	Hardness (HV)	EWF (eV)
LCA	190.81	117	4.632
LCN	196.33	133	4.701

4.2.3 Relationship between corrosion resistance and EWF

The corrosion behavior of a material is related to its electrochemical stability, which is related to the electron stability of atomic bonds. Thus, higher EWF should correspond to higher intrinsic corrosion resistance (*17*). Here, the intrinsic corrosion resistance does not include the influences from surface adsorption and oxidation, e.g., the formation of passive films. Or in other words, it refers to the resistance to material dissolution in a corrosive environment. Corrosion resistance can be evaluated by two parameters, one is the corrosion

rate (CR) which directly related to reaction kinetics and the other is the corrosion potential (E_{corr}) which reflects the corrosion tendency of a material or the driving force for starting corrosion. Based on Faraday's law (*88*), corrosion rate is represented as:

$$\text{Corrosion Rate(CR)} = \frac{k \times j_{corr} \times EW}{\rho} \quad (4.1)$$

where k is 0.00327 mm×g/(μA×cm×yr) for 3.5 wt.% NaCl salt solution, j_{corr} is corrosion current density (μA/cm^2), EW is equivalent weight of mild steel which is estimated to be 28.25. ρ is density of steel and set to be 7.86 g/cm^3 (*88*). In this study, 3.5 wt.% NaCl salt solution and a dilute HCL solution are used to investigate the corrosion resistances of LCA and LCN samples. In the NaCl solution, Cl^- plays a main role in corroding the steel, which is mainly influenced by pitting and intergranular corrosion effect (*89*). Figure 4.4A illustrates the open circuit potentials (OCP) of the two samples against time. As shown, the normalized sample has a higher OCP with less tendency of being corroded. Polarization curves of two samples are illustrated in figure 4.4B. Using extrapolation method, the corrosion potential and corrosion current density can be determined based on the polarization curve. Results of the measurement are given in table 4.2. As shown, the corrosion current density of LCN is lower than that of LCA, indicating that the LCN sample has a lower kinetic rate of corrosion in the salty solution. For more information, corrosion behaviors of the two samples in a 0.5M HCl acid solution were also analyzed, in which carbon steel generally dissolves without formation of a surface film that complicates the corrosion process. The dilute HCL acidic solution is usually used as an aggressive corrosion medium in industrial processes such as pickling and etching (*90*). Figure 4.4C and D show OCP and polarization curve of the two samples in the acidic solution,

respectively. The LCN sample still shows lower corrosion tendency, compared to that of the LCA sample, while their polarization curves are closer. Table 4.2 provides values of corrosion potential, corrosion current (I_{corr}), corrosion current density and corrosion rate of the two samples. As shown, the corrosion current density of LCN is lower than that of LCA but the percentage difference is not as large as that in the NaCl solution, since the carbon steel is more prone to the acidic solution.

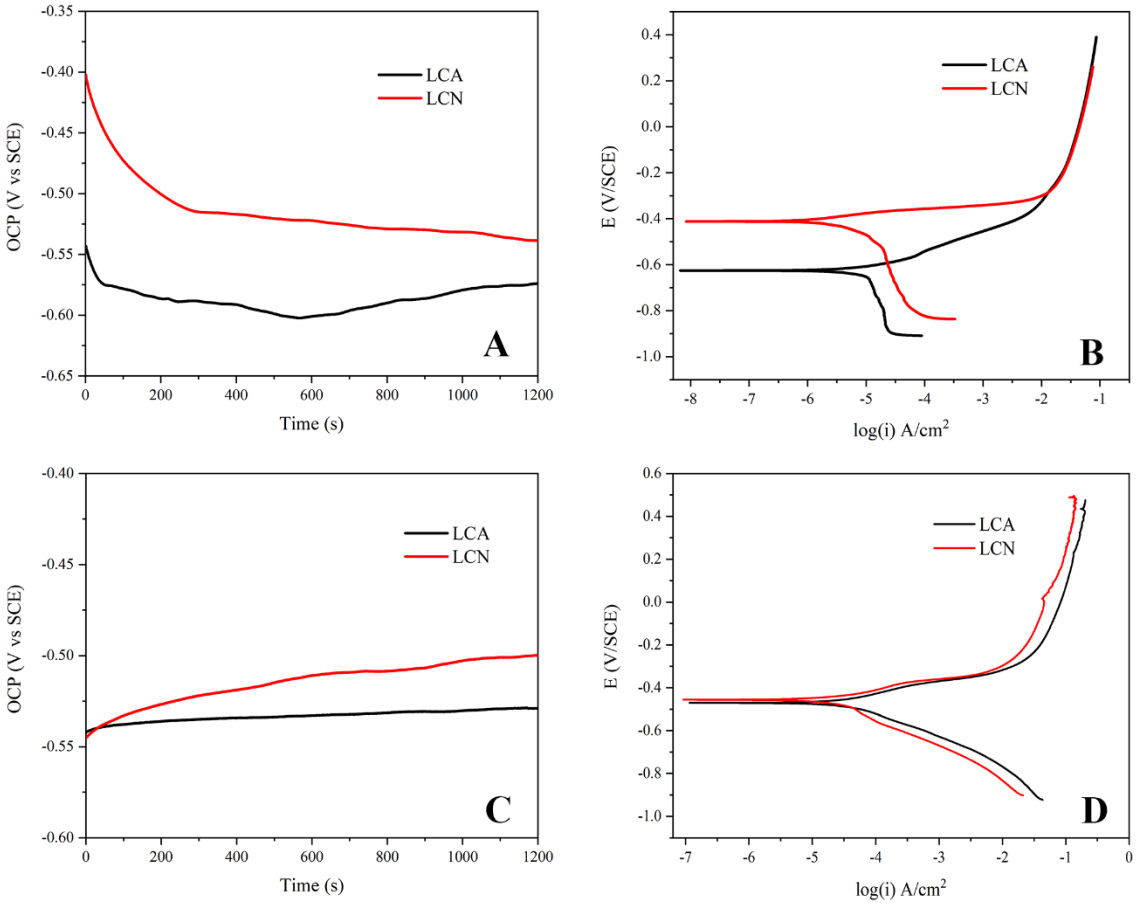

Figure 4.4 (A) Open circuit potential and (B) polarization curve in 3.5 wt. % NaCl solution; (C) Open circuit potential and (D) polarization curve in 0.5 mol/L HCl solution

Table 4.2 Corrosion potentials (E_{corr}), corrosion currents (I_{corr}), corrosion current densities (j_{corr}) and corrosion rates (CR) of LCA and LCN samples in the two different solutions

Solution	sample	E_{corr} /V	I_{corr} /μA	j_{corr} / (μA/cm^2)	CR / (mm/yr)
3.5 wt.% NaCl	LCA	-0.638	21.21	10.45	0.123
	LCN	-0.382	5.25	2.74	0.032
0.5 mol/L HCl	LCA	-0.466	30.01	25.47	0.299
	LCN	-0.416	28.69	14.96	0.176

Based on the measured corrosion parameters, the relationship between EWF and the corrosion resistance is clearly shown in figures 4.5 and 4.6. With higher overall EWF that corresponds to a more stable state of electrons, the LCN sample shows higher resistance to corrosion (lower CR and higher E_{corr}), compared with LCA sample in both the acidic and salty solutions.

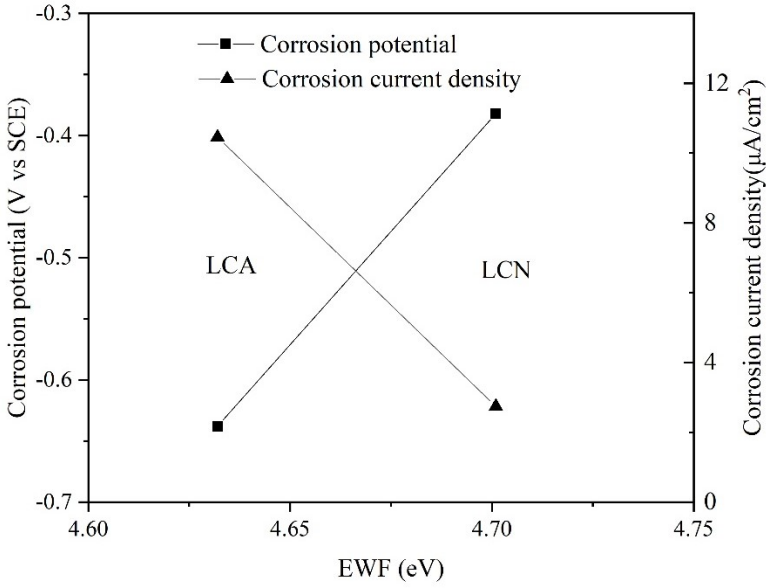

Figure 4.5 Relationship between EWF and corrosion potential, corrosion current density in 3.5 wt.% NaCl solution

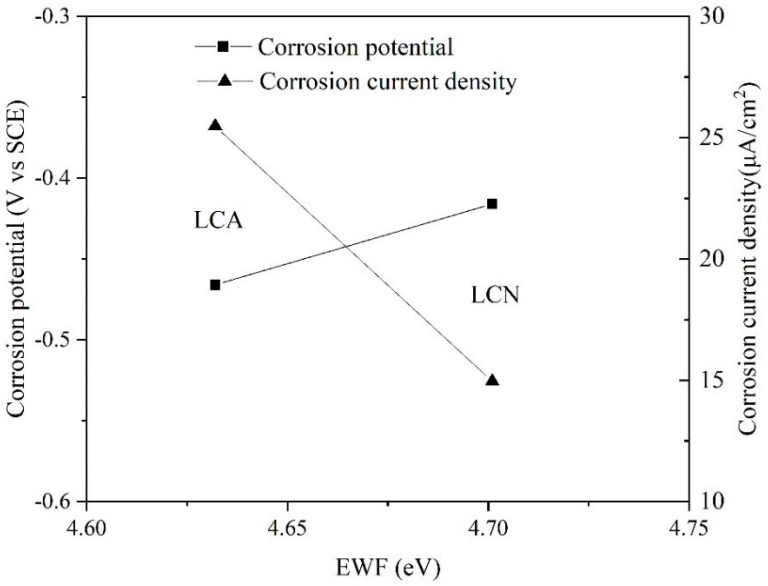

Figure 4.6 Relationship between EWF and corrosion potential, corrosion current density in 0.5 mol/L HCl solution

4.2.4 EWF of pearlite - a microconstituent consisting of cementite and ferrite

As already shown in figure 4.2, there are two levels of microstructural inhomogeneity in low carbon steel which may affect overall work function. Let's look at the pearlite first, which consists of two phases, ferrite (α-Fe) and cementite (Fe_3C). When two different phases are in contact, electrons move from the phase having a lower EWF to that with a high EWF, driven by a contact potential difference (*43*). In the present case, electrons in ferrite tend to move towards adjacent cementite that has a higher potential or EWF until a dipole layer is established at the Fe/Fe_3C interface. As shown in figure 4.7, electrons are accumulated at the interface, which would build an electric field within the interface region as the charge accumulation, generating an opposite electrostatic force to balance the driving force resulting from the contact potential difference (*91*). As electrons move towards the interfacial area, electrons are depleted in the ferrite region. Such charge relocation leads to a positively charged ferrite region, from which electrons would have increased difficulty to escape when under an external electrical field during EWF measurement. Equivalently, the measured EWF would be higher. The corresponding percentage increase in work function can be described with interfacial and volume parameters:

$$\frac{\Delta\varphi}{\varphi_{\text{initial}}} = \frac{\Delta\rho_{e-}}{6\rho_{e-}} = \frac{S\sigma}{6V\rho_{e-}} \tag{4.2}$$

With a higher S/V ratio or a finer microstructure, the measured EWF would be increased with correspondingly changed mechanical and electrochemical properties. (Detailed derivation is given in Chapter 3.2.4). When the steel is cooled at a higher cooling

rate, the thickness of plate-cementite in pearlite becomes finer with a larger S/V ratio. It is expected that the pearlite in the normalized sample would have a higher EWF than that of pearlite in the furnace-cooled sample in which the pearlite is coarser (see figures 4.2F and M). In order to confirm this, EWFs of pearlite domains in LCA and LCN samples were analyzed through AFM mapping. Figures 4.8 (A, B) and (C, D) show representative topographical maps of LCA and LCN samples, respectively. Corresponding potential maps of the samples are illustrated in figures 4.8 (E, F) and (G, H). The light areas represent pearlite (P) and the dark one represents ferrite matrix(F). Figures 4.8I and J show local potential variations between LCA and LCN measured along the white lines in E to H. Statistical results confirm that pearlite shows higher potential than ferrite, which can cause the electron redistribution at the interface. Table 4.3 gives the measured EWFs of perlite domains in LCA and LCN samples. As shown, EWF of the pearlite in LCN sample is higher than that in LCA sample, consistent with the theoretical analysis.

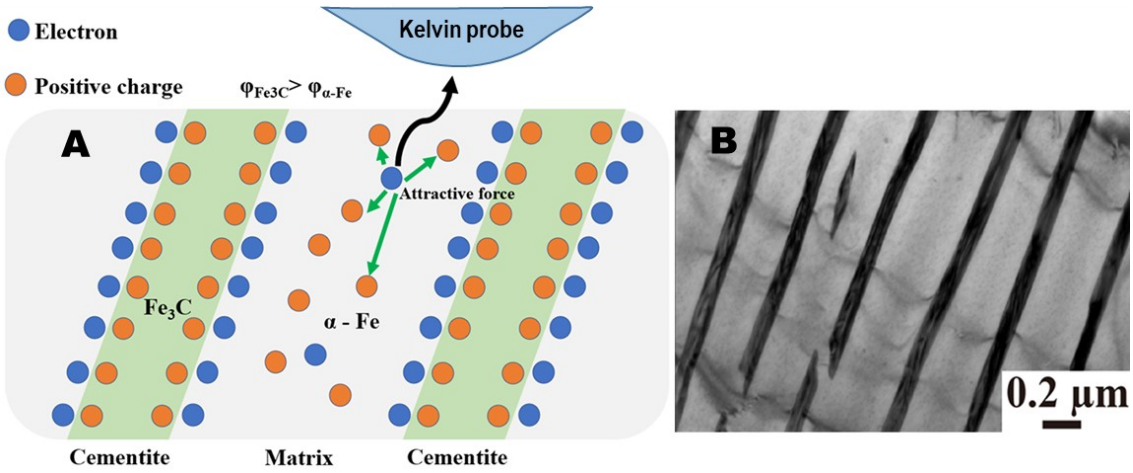

Figure 4.7 (A) Schematic of the charge - compensation model: electrons move towards the Fe/Fe_3C interface, building a dipole layer to stop further charge accumulation. The ferrite region becomes electron-depleted, (B) A TEM image of pearlite consisting ferrite and cementite (dark)

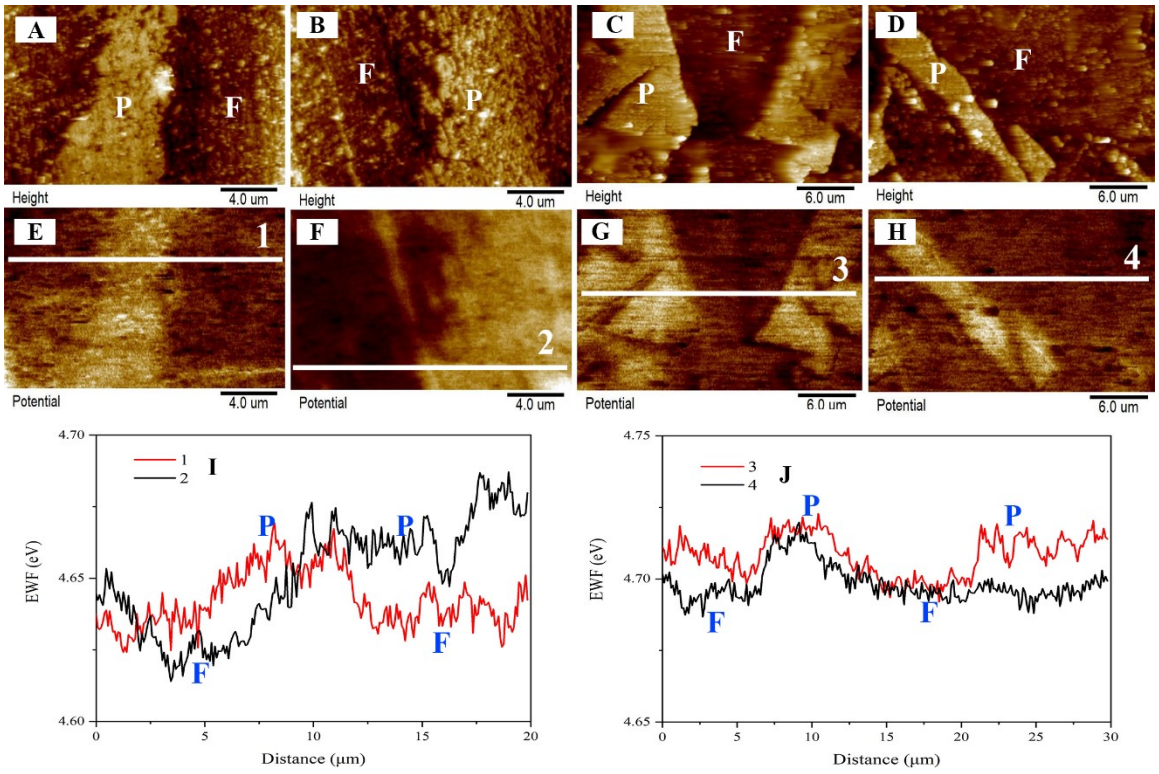

Figure 4.8 Topographical maps of (A, B) LCA and (C, D) LCN; P represents pearlite and F represents ferrite in the images; Corresponding potential maps of (E, F) LCA and (G, H) LCN; (I) Line profile of potential change (along lines 1 and 2 in figures E and F, respectively) in LCA, (J) Line profile of potential change (along lines 3 and 4 in figures G and H, respectively) in LCN

Table 4.3 Statistical local work function in LCA and LCN samples

Local Work Function (eV)	Pearlite	Matrix
LCA	4.66	4.63
LCN	4.72	4.69

4.2.5 EWF of the steel - an alloy system consisting of pearlite and ferrite

For the air-cooled and furnace-cooled samples, their microstructures are different at two levels. The microstructural difference at level one refers to the difference in size and spacing of cementite in pearlite between sample LCA and sample LCN as shown in figures 4.2G and N. The microstructural difference at level two refers to the difference in the sizes of pearlite and ferrite domains between the samples as figures 4.2A and H or figure 4.9 illustrate. Since pearlite has a higher EWF than ferrite matrix as figures 4.8I and J illustrate, a dipole layer would also form at the pearlite/ferrite interface. Thus, EWF of the samples would also be influenced by microstructure at this level involving the size of pearlite domains and the spacing between adjacent pearlite domains.

For the pearlite-ferrite microstructural inhomogeneity, interfacial charge density at pearlite/ferrite interface is defined and expressed as:

$$\sigma = \frac{2\varepsilon_0[\varphi\ (\text{pearlite}) - \ \varphi\ (\text{ferrite matrix})]}{x^2 e^2} \tag{4.3}$$

The principle of theoretical calculation is the same with Chapter 3.2.4. Based on obtained EWFs of pearlite and ferrite in LCA and LCN samples and their S/V ratios, theoretical interfacial charge density are calculated and presented in Table 4.4. As shown, σ shows similar value between LCA and LCN sample. Since the magnitude of change in work function is affected by the S/V ratio, for comparison purpose, we use the length of interfacial line over the cross-section area of ferrite phase to represent the S/V ratio. Figure 4.9 gives micrographs processed by Image-pro Plus. Interface between pearlite and matrix is drawn by red line. As shown in Table 4.4, S/V ratio increases significantly in LCN

sample, which is three times as high as that of LCA. This makes a main contribution to the charge compensation effect, leading to increased overall electronic stability. Free electron density ρ_{e-} is determined by density parameter r_s (Fe 1.04 Å) (*52*), so initial ferrite matrix's free electron density is set to be 2.12×10^{29} electrons/m^3. The increasing percentage of apparent work function is given in Table 4.4. LCN sample has its EWF increased by 2.3%, resulting from its fine and dense pearlite configuration, corresponding to better mechanical performance. If the initial work function of iron is set to be 4.5 eV (*52*), the theoretical overall EWF can be provided, which shows a good fit with experimental data. This microstructure – EWF – property model works well for the low-carbon steel with microstructural features.

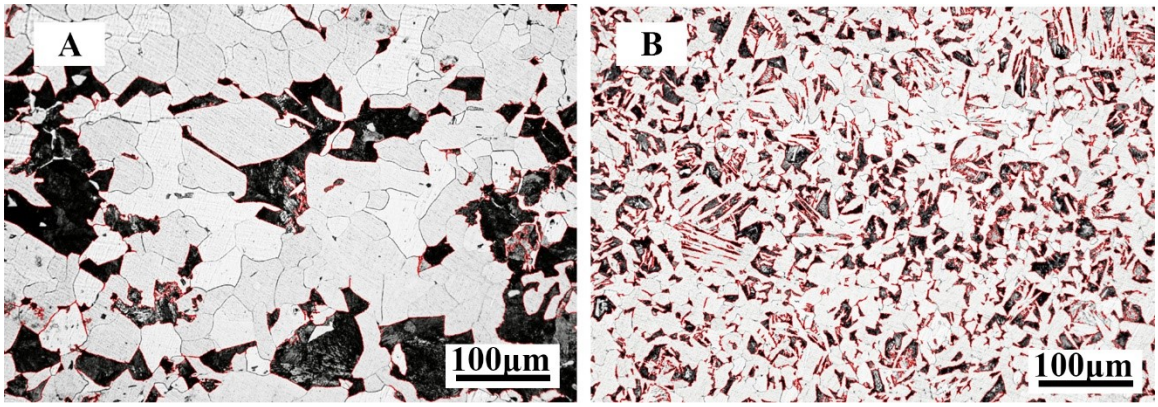

Figure 4.9 (A) Optical micrographs of LCA with red interfacial lines, (B) Optical micrographs of LCN with red interfacial lines

Table 4.4 Detailed data (e.g., interfacial charge density, S/V, etc.) used in model calculations

Sample	LCA	LCN
$\triangle\varphi$ (eV)	0.035	0.027
σ ($10^{23}/m^2$)	1.55	1.19
Percentage of pearlite (%)	0.2846	0.2445
Interfacial line (μm)	12219	41719
Matrix area (μm^2)	164899	174143
S/V ($10^6/m$)	0.074	0.240
$\triangle\varphi/\varphi_{initial}$ (%)	0.90	2.25
$\varphi_{theoretical}$ (eV)	4.541	4.601
$\varphi_{measured}$ (eV)	4.632	4.701

4.3 Conclusions

For the study presented in Chapter 4, the following conclusions are drawn:

1) The normalized sample (LCN) has pearlite containing thinner cementite plates embedded in ferrite with a smaller spacing between adjacent cementite plates. The pearlite in LCN shows a higher EWF, compared to that in the furnace-cooled sample (LCA).
2) The LCN sample has a finer microstructure with smaller pearlite (P) and ferrite (F) domains and its total P/F interfacial area is considerably larger than that in LCA, resulting in further increased EWF. The normalized sample has a higher overall EWF

than the furnace-cooled sample.

3) When two microconstituents having different EWFs are in contact, electrons move from the low-EWF one to that having a higher EWF until the formed dipole layer at the interface is sufficiently strong to stop the electron redistribution. Equivalently the low-EWF microconstituent becomes positively charged, leading to enhanced confinement to electrons and thus elevated apparent EWF.
4) Higher apparent EWF corresponds to stronger overall confinement to electrons, resulting in stronger atomic bonding and stability, corresponding to higher mechanical strength and higher resistance to corrosion.

Up to this point, we demonstrate that the apparent EWF does carry the information on integrated electron behavior and overall properties of multiphase alloys. Establishment of such relationships is a crucial step towards the design of structural materials on a feasible electronic base or through “electronic metallurgy” as a complementary or alternative methodology.

Chapter 5 General conclusions and future studies

5.1 Conclusions

Electron work function is a promising parameter for designing structural materials. This parameter is intrinsically related to the metallic bonding and thus mechanical and electrochemical properties of metals. However, whether EWF can reflect overall properties of a multiphase alloy, which are integrated from those of individual phases, is a main barrier to the application of EWF in material design towards a more fundamental metallurgical framework: "electronic metallurgy". In this thesis, we demonstrate that the apparent EWF does carry the information on integrated electron behavior and overall properties of multiphase alloys. The detailed conclusions are listed below:

- EWF has been correlated well with atomic bonding, physical and mechanical properties of homogeneous solid solutions both theoretically and experimentally.
- A charge-compensation model is established to explain the change of overall EWF, which is affected by the microstructural arrangement between different phases. In addition to the difference in EWF between different phases, the interface plays a crucial role in influencing the overall EWF.
- Using high-Cr cast irons as a sample material, we demonstrate that the apparent EWF of the multiphase alloy reflects the integrated electron behavior and Young's modulus.
- Low carbon steel having two levels of microstructure inhomogeneity is used to further verify this model. With higher electronic stability, mechanical properties such as

Young's modulus and hardness increase accordingly, and so does the corrosion resistance.

- Microstructure – EWF – property relationships are studied towards an alternative or supplementary methodology for material design and development.

5.2 Future studies

- In the process of calculating theoretical EWF, we selected the most commonly used parameters for calculation. More accurate data can be obtained if first-principles calculation is applied to interfacial charge density analysis. More details about the charge redistribution and the mechanism could be obtained and better understood.
- Surface condition affects the measurement of EWF. For instance, oxidation, roughness, and defects introduced during surface preparation of samples would more or less affect the accuracy of EWF. How to minimize these effects need to be investigated.
- EWF are mostly applied to metallic products so far. Applications of EWF in analyzing ceramic and polymers are rather limited. Preliminary studies have shown that EWF can be applied to some ceramic materials with metallic bond components. Further studies are needed in order to extend the application of EWF in materials research and development.

References

1. N. Lang, W. Kohn, Theory of metal surfaces: work function. *Physical Review B* **3**, 1215 (1971).
2. S. Hałas, 100 years of work function. *Materials Science-Poland* **24**, 951-968 (2006).
3. H. L. Skriver, N. Rosengaard, Surface energy and work function of elemental metals. *Physical Review B* **46**, 7157 (1992).
4. G. Samsonov, V. Fomenko, I. Podchernyaeva, L. Okhremchuk, Thermionic emission properties of refractory compounds and materials based on them (a review). *Soviet Powder Metallurgy and Metal Ceramics* **13**, 836-842 (1974).
5. A. Miedema, The electronegativity parameter for transition metals: heat of formation and charge transfer in alloys. *Journal of the less common metals* **32**, 117-136 (1973).
6. H. B. Michaelson, Relation between an atomic electronegativity scale and the work function. *IBM Journal of research and development* **22**, 72-80 (1978).
7. G. Hua, D. Li, Generic relation between the electron work function and Young's modulus of metals. *Applied Physics Letters* **99**, 041907 (2011).
8. G. Hua, D. Li, The correlation between the electron work function and yield strength of metals. *physica status solidi (b)* **249**, 1517-1520 (2012).
9. G. Hua, D. Li, Electron work function: a novel probe for toughness. *Physical Chemistry Chemical Physics* **18**, 4753-4759 (2016).
10. K. KALAZHOKOV, A. Gonov, Z. Kalazhokov, On the calculation of the surface energy of a face of a single crystal through the electron work function of this face.

Russian metallurgy. Metally, 39-41 (1996).

11. L. Guo, G. Hua, B. Yang, H. Lu, L. Qiao, X. Yan, D. Li, Electron work functions of ferrite and austenite phases in a duplex stainless steel and their adhesive forces with AFM silicon probe. *Scientific reports* **6**, 20660 (2016).
12. Y. Li, D. Li, Electron work function, adhesion, and friction between 3d transition metals under light loads. *Wear* **259**, 1432-1436 (2005).
13. Y. Li, D. Li, Experimental studies on relationships between the electron work function, adhesion, and friction for 3d transition metals. *Journal of applied physics* **95**, 7961-7965 (2004).
14. J. A. Rothschild, M. Eizenberg, Work function calculation of solid solution alloys using the image force model. *Physical Review B* **81**, 224201 (2010).
15. H. Lu, G. Hua, D. Li, Dependence of the mechanical behavior of alloys on their electron work function—An alternative parameter for materials design. *Applied Physics Letters* **103**, 261902 (2013).
16. X. Huang, H. Lu, H. He, X. Yan, D. Li, Correlation between the wear resistance of Cu-Ni alloy and its electron work function. *Philosophical Magazine* **95**, 3896-3909 (2015).
17. X. Huang, H. Lu, D. Li, Understanding the corrosion behavior of isomorphous Cu–Ni alloy from its electron work function. *Materials Chemistry and Physics* **173**, 238-245 (2016).
18. O. Bouaziz, S. Allain, C. Scott, P. Cugy, D. Barbier, High manganese austenitic twinning induced plasticity steels: A review of the microstructure properties relationships. *Current opinion in solid state and materials science* **15**, 141-168

(2011).

19. S. C. Tjong, Z. Ma, Microstructural and mechanical characteristics of in situ metal matrix composites. *Materials Science and Engineering: R: Reports* **29**, 49-113 (2000).

20. Y. Zhang, T. T. Zuo, Z. Tang, M. C. Gao, K. A. Dahmen, P. K. Liaw, Z. P. Lu, Microstructures and properties of high-entropy alloys. *Progress in Materials Science* **61**, 1-93 (2014).

21. Y. Wang, M. Chen, F. Zhou, E. Ma, High tensile ductility in a nanostructured metal. *Nature* **419**, 912-915 (2002).

22. A. Iza-Mendia, I. Gutiérrez, Generalization of the existing relations between microstructure and yield stress from ferrite–pearlite to high strength steels. *Materials Science and Engineering: A* **561**, 40-51 (2013).

23. D. Li, L. Guo, L. Li, H. Lu, Electron work function–a probe for interfacial diagnosis. *Scientific reports* **7**, 1-8 (2017).

24. S. Mosleh-Shirazi, G. Hua, F. Akhlaghi, X. Yan, D. Li, Interfacial valence electron localization and the corrosion resistance of Al-SiC nanocomposite. *Scientific reports* **5**, 18154 (2015).

25. H. Lu, X. Huang, R. Hou, D. Li, Understanding the Effect of Ni on Mechanical and Wear Properties of Low-Carbon Steel from a View-Point of Electron Work Function. *Metallurgical and Materials Transactions A* **49**, 2612-2621 (2018).

26. P. A. M. Dirac, The quantum theory of the electron. *Proceedings of the Royal Society of London. Series A, Containing Papers of a Mathematical and Physical Character* **117**, 610-624 (1928).

27. P. A. M. Dirac, Quantum mechanics of many-electron systems. *Proceedings of the Royal Society of London. Series A, Containing Papers of a Mathematical and Physical Character* **123**, 714-733 (1929).

28. H. A. Bethe, E. E. Salpeter, *Quantum mechanics of one-and two-electron atoms*. (Springer Science & Business Media, 2012).

29. J. Bardeen, Theory of the work function. II. The surface double layer. *Physical Review* **49**, 653 (1936).

30. R. Smoluchowski, Anisotropy of the electronic work function of metals. *Physical Review* **60**, 661 (1941).

31. P. Hofmann, *Solid state physics: an introduction*. (John Wiley & Sons, 2015).

32. C. Kittel, P. McEuen, P. McEuen, *Introduction to solid state physics*. (Wiley New York, 1996), vol. 8.

33. H. Ishii, K. Sugiyama, E. Ito, K. Seki, Energy level alignment and interfacial electronic structures at organic/metal and organic/organic interfaces. *Advanced materials* **11**, 605-625 (1999).

34. E. Wigner, J. Bardeen, in *Part I: Physical Chemistry. Part II: Solid State Physics*. (Springer, 1997), pp. 398-401.

35. T. Leung, C. Kao, W. Su, Y. Feng, C. Chan, Relationship between surface dipole, work function and charge transfer: Some exceptions to an established rule. *Physical Review B* **68**, 195408 (2003).

36. W. Li, D. Li, Influence of surface morphology on corrosion and electronic behavior. *Acta materialia* **54**, 445-452 (2006).

37. D. Li, Electron work function at grain boundary and the corrosion behavior of

nanocrystalline metallic materials. *MRS Online Proceedings Library Archive* **887**, (2005).

38. J. Janata, Chemical modulation of the electron work function. *Analytical Chemistry* **63**, 2546-2550 (1991).

39. P. S. Bagus, D. Käfer, G. Witte, C. Wöll, Work function changes induced by charged adsorbates: origin of the polarity asymmetry. *Physical review letters* **100**, 126101 (2008).

40. L. Kelvin, V. Contact electricity of metals. *The London, Edinburgh, and Dublin Philosophical Magazine and Journal of Science* **46**, 82-120 (1898).

41. J. Stein, An Improved Method for Constructing Electrostatic Prisms. *Review of Scientific Instruments* **41**, 477-477 (1970).

42. M. Rohwerder, F. Turcu, High-resolution Kelvin probe microscopy in corrosion science: scanning Kelvin probe force microscopy (SKPFM) versus classical scanning Kelvin probe (SKP). *Electrochimica Acta* **53**, 290-299 (2007).

43. N. Surplice, R. D'arcy, A critique of the Kelvin method of measuring work functions. *Journal of Physics E: Scientific Instruments* **3**, 477 (1970).

44. Y. Park, V. Choong, Y. Gao, B. R. Hsieh, C. W. Tang, Work function of indium tin oxide transparent conductor measured by photoelectron spectroscopy. *Applied physics letters* **68**, 2699-2701 (1996).

45. M. Nonnenmacher, M. o'Boyle, H. K. Wickramasinghe, Kelvin probe force microscopy. *Applied physics letters* **58**, 2921-2923 (1991).

46. W. Melitz, J. Shen, A. C. Kummel, S. Lee, Kelvin probe force microscopy and its application. *Surface science reports* **66**, 1-27 (2011).

47. L. Guo, L. Li, Q. Li, W. Li, D. Chen, D. Li, In Situ AFM Analysis of Surface Electron Behaviors of Strain-Free and Deformed Ferrite and Austenite in Duplex Steel and Their Correlation with Electron Work Function. *physica status solidi (a)* **216**, 1800933 (2019).

48. I. Brodie, Uncertainty, topography, and work function. *Physical Review B* **51**, 13660 (1995).

49. H. Lu, D. Li, Correlation between the electron work function of metals and their bulk moduli, thermal expansion and heat capacity via the Lennard–J ones potential. *physica status solidi (b)* **251**, 815-820 (2014).

50. Z. Liu, D. Li, The electronic origin of strengthening and ductilizing magnesium by solid solutes. *Acta Materialia* **89**, 225-233 (2015).

51. C. Lung, N. H. March, *Mechanical Properties of Metals: Atomistic and Fractal Continuum Approaches*. (World Scientific, 1999).

52. S. Halas, T. Durakiewicz, Work functions of elements expressed in terms of the Fermi energy and the density of free electrons. *Journal of Physics: Condensed Matter* **10**, 10815 (1998).

53. H. B. Michaelson, The work function of the elements and its periodicity. *Journal of applied physics* **48**, 4729-4733 (1977).

54. J. Bray, ASM Handbook, vol. 2: Properties and Selection: Nonferrous Alloys and Special-Purpose Materials. *ASM International, Materials Park, OH*, 29-61 (1990).

55. J. Hirth, J. Lothe, Theory of Dislocations, Wiley, New York 1982. (1982).

56. A. C. Fischer-Cripps, in *Nanoindentation*. (Springer, 2002), pp. 159-173.

57. M. Brajczewska, C. Henriques, C. Fiolhais, Dependence of metal surface properties

on the valence-electron density in the stabilized jellium model. *Vacuum* **63**, 135-138 (2001).

58. D.-P. Ji, Q. Zhu, S.-Q. Wang, Detailed first-principles studies on surface energy and work function of hexagonal metals. *Surface Science* **651**, 137-146 (2016).

59. A. Noy, C. D. Frisbie, L. F. Rozsnyai, M. S. Wrighton, C. M. Lieber, Chemical force microscopy: exploiting chemically-modified tips to quantify adhesion, friction, and functional group distributions in molecular assemblies. *Journal of the American Chemical Society* **117**, 7943-7951 (1995).

60. H. Lu, X. Huang, D. Li, Understanding the bond-energy, hardness, and adhesive force from the phase diagram via the electron work function. *Journal of Applied Physics* **116**, 173506 (2014).

61. E. Iguchi, K. Udagawa, Analysis of Young's modulus in the polycrystalline Cu-Ni alloy with the theory for Nordheim's rule. *Journal of Physics F: Metal Physics* **5**, 214 (1975).

62. I. Hutchings, 'Tribology: friction and wear of engineering materials'; 1992, London, Edward Arnold.

63. H. Lu, Z. Liu, X. Yan, D. Li, L. Parent, H. Tian, Electron work function–a promising guiding parameter for material design. *Scientific reports* **6**, 1-11 (2016).

64. N. Mott, F. N. Nabarro, An attempt to estimate the degree of precipitation hardening, with a simple model. *Proceedings of the Physical Society* **52**, 86 (1940).

65. R. L. Fleisgher, Solution hardening. *Acta metallurgica* **9**, 996-1000 (1961).

66. F. Nabarro, Report of a conference on the strength of solids. *The Physical society*, London, (1948).

67. H. Lu, L. Li, X. Huang, D. Li, An electron work function based mechanism for solid solution hardening. *Journal of Alloys and Compounds* **737**, 323-329 (2018).

68. I. Lundström, S. Shivaraman, C. Svensson, L. Lundkvist, A hydrogen− sensitive MOS field− effect transistor. *Applied Physics Letters* **26**, 55-57 (1975).

69. C. Benndorf, G. Klatte, F. Thieme, Interaction of oxygen with CuNi (110) alloy surfaces: AES, XPS and work function measurements. *Surface science* **135**, 1-17 (1983).

70. A. Oprea, N. Bârsan, U. Weimar, Work function changes in gas sensitive materials: Fundamentals and applications. *Sensors and Actuators B: Chemical* **142**, 470-493 (2009).

71. X. Wang, T. Jones, Y. Wu, Z. Lu, S. Halas, T. Durakiewicz, M. Eberhart, An electronic criterion for assessing intrinsic brittleness of metallic glasses. *The Journal of chemical physics* **141**, 024503 (2014).

72. R. H. Baughman, J. M. Shacklette, A. A. Zakhidov, S. Stafström, Negative Poisson's ratios as a common feature of cubic metals. *Nature* **392**, 362-365 (1998).

73. H. Lu, C. Ouyang, X. Yan, J. Wang, G. Hua, R. Chung, D. Li, Potential application of electron work function in analyzing fracture toughness of materials. *Journal of materials science & technology* **33**, 1128-1133 (2017).

74. J. Gilman, R. Cumberland, R. Kaner, Design of hard crystals. *International Journal of Refractory Metals and Hard Materials* **24**, 1-5 (2006).

75. H. Niu, X.-Q. Chen, P. Liu, W. Xing, X. Cheng, D. Li, Y. Li, Extra-electron induced covalent strengthening and generalization of intrinsic ductile-to-brittle criterion. *Scientific reports* **2**, 1-6 (2012).

76. F. Giustino, *Materials modelling using density functional theory: properties and predictions*. (Oxford University Press, 2014).

77. G. Kresse, J. Hafner, Ab initio molecular dynamics for liquid metals. *Physical Review B* **47**, 558 (1993).

78. G. Kresse, J. Furthmüller, Efficient iterative schemes for ab initio total-energy calculations using a plane-wave basis set. *Physical review B* **54**, 11169 (1996).

79. G. Kresse, D. Joubert, From ultrasoft pseudopotentials to the projector augmented-wave method. *Physical review b* **59**, 1758 (1999).

80. J. P. Perdew, K. Burke, M. Ernzerhof, Generalized gradient approximation made simple. *Physical review letters* **77**, 3865 (1996).

81. H. J. Monkhorst, J. D. Pack, Special points for Brillouin-zone integrations. *Physical review B* **13**, 5188 (1976).

82. K. Wang, D. Li, Formation of core (M7C3)-shell (M23C6) structured carbides in white cast irons: A thermo-kinetic analysis. *Computational Materials Science* **154**, 111-121 (2018).

83. J. C. Francken, Analogical methods for resolving Laplace's and Poisson's equations. *Focusing of charged particles* **1**, 101-162 (1967).

84. L. Genovese, T. Deutsch, A. Neelov, S. Goedecker, G. Beylkin, Efficient solution of Poisson's equation with free boundary conditions. *The Journal of chemical physics* **125**, 074105 (2006).

85. K. Teng, S. Li, Theoretical calculations of Debye length, built-in potential and depletion layer width versus dopant density in a heavily doped pn junction diode. *Solid-state electronics* **28**, 277-285 (1985).

86. D. H. Shin, B. C. Kim, K.-T. Park, W. Y. Choo, Microstructural changes in equal channel angular pressed low carbon steel by static annealing. *Acta Materialia* **48**, 3245-3252 (2000).

87. Q. Li, G. Hua, H. Lu, B. Yu, D. Li, Understanding the effect of plastic deformation on elastic modulus of metals based on a percolation model with electron work function. *JOM* **70**, 1130-1135 (2018).

88. O. Sekunowo, S. Adeosun, G. Lawal, Potentiostatic polarisation responses of mild steel in seawater and acid environments. *International Journal of Scientific and Technology Research* **2**, (2013).

89. G.-L. Song, D. Haddad, The topography of magnetron sputter-deposited Mg–Ti alloy thin films. *Materials Chemistry and Physics* **125**, 548-552 (2011).

90. E. Gutiérrez, J. A. Rodríguez, J. Cruz-Borbolla, J. G. Alvarado-Rodríguez, P. Thangarasu, Development of a predictive model for corrosion inhibition of carbon steel by imidazole and benzimidazole derivatives. *Corrosion Science* **108**, 23-35 (2016).

91. S. S. Li, *Semiconductor physical electronics*. (Springer Science & Business Media, 2012).